This article has been accepted to Earth and Planetary Science Letters and is currently in post-production

Bayesian inference on the initiation phase of the 2014 Iquique, Chile, earthquake

Cedric Twardzik[1,a], Zacharie Duputel[2], Romain Jolivet[3], Emilie Klein[3], and Paul Rebischung[4]

[1]Institut Terre et Environnement Strasbourg, Université de Strasbourg, EOST, CNRS UMR 7063, 5 rue Descartes, F-67084, Strasbourg, France
[2]Observatoire Volcanologique du Piton de la Fournaise, Universite de Paris, Institut de Physique du Globe de Paris, CNRS, F-75005, Paris, France
[3]Laboratoire de Géologie, CNRS UMR 8538, École Normale Supérieure, PSL University, Institut Universitaire de France, 1 rue Descartes, 75006, Paris, France
[4]Université de Paris, Institut de Physique du Globe de Paris, CNRS, IGN, France, ENSG-Géomatique, IGN, Marne-la-Vallée, France
[a]now at: Université Côte d'Azur, CNRS, Observatoire de la Côte d'Azur, IRD, Geoazur, UMR 7329, Valbonne, France

Correspondence: Cedric Twardzik (twardzik@geoazur.unice.fr)

Abstract. We investigate the initiation phase of the 2014 M_w8.1 Iquique earthquake in northern Chile. In particular, we focus on the month preceding the mainshock, a time period known to exhibit an intensification of the seismic and aseismic activity in the region. The goal is to estimate the time-evolution and partitioning of seismic and aseismic slip during the preparatory phase of the mainshock. To do so, we develop a Bayesian inversion scheme to infer the spatio-temporal evolution of pre-slip from position time-series along with the corresponding uncertainty. To extract the aseismic component to the pre-seismic motion, we correct geodetic observations from the displacement induced by foreshocks. We find that aseismic slip accounts for $\sim$20 percents of the slip budget. That aseismic slip takes the form of a slow-slip events occurring between 20 to 5 days before the future mainshock. This time-evolution is not consistent with self-accelerating fault slip, a model that is often invoked to explain earthquake nucleation. Instead, the slow-slip event seems to have interacted with the foreshock sequence such that the foreshocks contributed to the arrest of aseismic slip. In addition, we observe some evidence of late self-accelerating slip, but associated with large uncertainties, making it difficult to assess its reliability from our observations alone.

1 Introduction

How an earthquake starts still remains a highly debated question (e.g., Gomberg, 2018). The initiation phase of the earthquake rupture is most often explained through one of these two conceptual models: the cascade model and the slow-slip model (e.g., Ellsworth and Beroza, 1995). In the former, it is proposed that a series of small earthquakes trigger one another in a close vicinity until one eventually triggers what becomes the mainshock (e.g., Brune, 1979; Ellsworth and Bulut, 2018). In the latter model, a large earthquake is believed to be preceded by the growth of a smoothly accelerating slow-slip event that eventually reaches typical co-seismic slip-rate (e.g., Ohnaka, 1992; Iio, 1995; Tape et al., 2018). More recently, hybrid models have also started to emerge. For instance, McLaskey (2019) has proposed that a self-accelerating slow-slip event drives the foreshocks activity, and that one of the foreshock eventually triggers the mainshock. Observation of the initiation phase remains very sparse, most of the earthquakes exhibiting no observable sign of a precursory phase. There are some rare examples, such as the 2014 Iquique, Chile, earthquake. Yet, there is still much debate about which of these different models best explain how this event has started.

On April 1, 2014, in northern Chile, near the city of Iquique, a M_w8.1 earthquake took place on the plate interface between the oceanic Nazca plate and the continental South American plate in the so-called North Chilean seismic gap. Indeed, prior to April 2014, no major earthquakes occurred in this region since 1877 (magnitude $\sim$8.6 – Comte and Pardo, 1991), and it was inferred from Global Navigation Satellite System (GNSS) that this part of the subduction interface was locked (Métois et al., 2013).

Seismic and geodetic networks in the region suggested that the plate interface started to slip $\sim$8 months prior to the Iquique earthquake, a motion that clearly intensified in the last few weeks before the mainshock (Socquet et al., 2017). Based on the surface observations, different interpretations were proposed to explain the physical origin of that pre-mainshock activity. Some authors suggested that the primary cause of the pre-mainshock geodetic motion was seismic slip induced by the numerous foreshocks recorded over the couple of weeks preceding the Iquique earthquake (Schurr et al., 2014), and that any potential aseismic slip would correspond to the post-seismic phase following these foreshocks (Bedford et al., 2015). Using tilt records along the GNSS data corrected from the contribution of the foreshocks, Boudin et al. (2019) also reached the conclusion that it was unlikely that a large slow-slip occurred near the epicentral region of the future Iquique earthquake, and that if so, it should have a magnitude of less than 6.6. From that angle, the initiation phase was more likely to be in line with the cascade model. However, it was also proposed that the pre-mainshock activity was due to a slow-slip event, located in the vicinity of the future mainshock, and which served as the driving mechanism of the foreshocks (Ruiz et al., 2014). From this point of view, the initiation was rather interpreted as the occurrence of a slow-slip model. This view was also shared by Meng et al. (2015) who studied earthquake repeaters to show the presence of a slow-slip event. Therefore, regarding the partitioning between seismic and aseismic slip during the initiation phase of the Iquique earthquake, these two interpretations stood on opposite side: one suggesting that the primary mode of slipping was seismic slip, and one suggesting that it was aseismic slip. However, others proposed that the seismic/aseismic slip partitioning was more balanced. For instance, Kato et al. (2016) estimated that seismic and aseismic slip were of the same order during the nucleation phase of the Iquique earthquake. Meanwhile, Socquet et al. (2017) estimated that aseismic slip accounted for $\sim$35% of the total slip on the plate interface over the last two weeks before the mainshock.

Because of these different interpretations about the seismic/aseismic slip partitioning, it is of particular interest to revisit the initiation phase of the Iquique earthquake under a Bayesian framework, which has the advantage of providing an ensemble of models for the partitioning along with a complete assessment of its uncertainty. Using that framework we aim not only at inferring the spatial pattern of preslip (i.e., the combined pre-mainshock seismic/aseismic slip) but also its temporal evolution. Knowing the spatio-temporal evolution is key to understand the relationship between seismic and aseismic slip during the initiation phase, but the temporal evolution can also help us to discriminate between post-seismic slip from the foreshocks and a self-accelerating slow-slip, both phenomena having very different temporal signatures (i.e., deceleration and acceleration of the slip-rate, respectively).

Thus, we use geodetic surface observations to infer the spatial and temporal evolution of preslip. We focus on the last month before the mainshock, when the seismic and geodetic activity is the strongest. At first, we are not making any assumptions as to the physical origin of the preslip since we are using geodetic observations that record the combined contribution of seismic and aseismic slip. Then, we correct these geodetic observations for the contribution of the foreshocks at the surface as an attempt to isolate aseismic slip. By comparing the results obtained from the two sets of observations (uncorrected and corrected), we infer the slip partitioning during the initiation phase of the Iquique earthquake. Finally, we discuss the physical origin of aseismic slip prior to the mainshock.

2 Time-dependent slip inversion

In order to obtain a detailed view of the spatio-temporal evolution of slip on the plate interface during the initiation phase of the Iquique earthquake, we have developed a time-dependent slip inversion scheme. As we want to assess the slip model uncertainty, the inversion is carried out under a Bayesian framework. In the following, we describe how we setup the forward model, i.e., how we build a time-dependent spatially variable preslip model that is used to compute the predictions of surface displacements.

2.1 The forward model

Throughout this study, we assume that all signals observed at the surface are caused by slip on the plate interface. In order to design a realistic plate interface, we mesh the Slab2.0 model (Hayes et al., 2018) using triangles for an accurate modelling of the geometry of the subducting slab. We end up with 27 nodes that make up the fault mesh (Figure 1a). The average spacing between the nodes is 150 km, meaning that a node has a dominant influence within 75 km with respect to the surrounding nodes. This distance is consistent with the size of the smallest resolvable feature estimated by Williamson and Newman (2018). They found it to be ∼80 km or more, offshore of Iquique, Chile, when using GNSS data alone.

The temporal evolution of slip at a given node is parametrized using a multi-time-window approach, similar to what has been developed for the study of the earthquake rupture (e.g., Olson and Aspel, 1982). Using that, the source time function, i.e., the function describing the temporal evolution of slip, is subdivided into several time windows (Figure 1b). Each one is weighted by the amount of slip representing its contribution to the total slip history (Figure 1c). This way, it is possible to construct a relatively complicated source time function. In mathematical form, the temporal evolution of slip $u(t)$ at a given fault node i is given by the following formula:

$$u_i(t) = \sum_{j=1}^{N_b} \phi_{ij} . \tau_j(t) \quad (1)$$

$\tau_j(t)$ represents the series of N_b basis functions, which describes how slip evolves as a function of time within a given time window j. We choose to use i-spline functions, which are monotonic and integrate to one. These two conditions ensure the positivity of slip when constraining the scaling coefficients (ϕ_{ij}) to be positive. The source time function at a given node is divided into 17 time windows (N_b=17), i.e., one starting every two days. Since we have 27 nodes, 459 model parameters are required to describe the spatial and temporal evolution of slip on the plate interface. We choose to reduce the temporal resolution so that the number of unknown (459) is relatively smaller than the number of data points (1394). This ensures a well determined problem and reduces the influence of the chosen prior distributions on the posterior distributions.

2.2 The inverse problem

Following Bayes' rule, the posterior probability density function can be approximated by:

$$p(\mathbf{m}|\mathbf{d}) \propto p(\mathbf{m})p(\mathbf{d}|\mathbf{m}), \tag{2}$$

where $p(\mathbf{m})$ is the prior probability density function, describing the knowledge that we have about the model parameters $\mathbf{m}$ before considering the data. $p(\mathbf{d}|\mathbf{m})$ is the data likelihood, which quantifies how well a given model satisfies the data $\mathbf{d}$. Here, we assume the gaussian form for the data likelihood:

$$p(\mathbf{d}|\mathbf{m}) \sim \exp\left[-\frac{1}{2}(\mathbf{d}-\mathbf{Gm})^{\mathrm{T}}\mathbf{C}_{\chi}^{-1}(\mathbf{d}-\mathbf{Gm})\right]. \tag{3}$$

In this formula, $\mathbf{G}$ is the response to slip on the fault at the data points, and it is computed using the CSI package (http://www.geologie.ens.fr/jolivet/csi) that incorporates the method of Zhu and Rivera (2012) for the calculation of static displacements in a layered model taken from Husen et al. (1999). We rotate the strike-slip and dip-slip components of $\mathbf{G}$ so that the latter is oriented along the plate convergence vector given by the MORVEL model (DeMets et al., 2010), and we only use the component that is oriented along the direction of the plate convergence vector.

$\mathbf{C}_\chi$ is the covariance matrix in the data space. It is composed of two terms summed together: the data covariance matrix $\mathbf{C}_d$, describing observational uncertainties, and the prediction covariance matrix $\mathbf{C}_p$, representing forward model uncertainty (also referred to as epistemic uncertainty). For the former, we refer the reader to the next section for explanation on how it is built. For the latter, we consider the effect that an incorrect knowledge of the Earth elastic properties has on the predictions. To compute $\mathbf{C}_p$, we use the formalism of Duputel et al. (2014):

$$\mathbf{C}_p = \mathbf{K}_\Omega.\mathbf{C}_\Omega.\mathbf{K}_\Omega^T \tag{4}$$

Here, $\mathbf{K}_\Omega$ represents the sensitivity kernel of the predictions with respect the Earth elastic properties Ω. $\mathbf{C}_\Omega$ represents the mean and covariance of the Earth elastic parameters, assuming that they follow log-normal distributions, which, as stated by Duputel et al. (2014), is justified by the fact that tomographic models are often obtained from relative model perturbations. $\mathbf{C}_\Omega$, is set so that the mean values are equivalent to the elastic parameters given by the Earth model of Husen et al. (1999). From the comparison with other models obtained in the region (Husen et al., 1999; Lüth, 2000; Legrand et al., 2007; Laske et al., 2013), we choose to use 6% of the mean value as the standard deviation for each layer, except for the top one for which we choose 10%. Aside the intrinsic uncertainty of the elastic parameters of our 1D velocity model, there is also uncertainty related to the fact that we use a simple 1D model instead of a model that accounts for the potential asymmetry of the velocity structure accross the slab interface. Indeed, it has been shown that using the later type of model has an impact on the predicted surface displacements (e.g., Masterlark, 2003). However, the epistemic uncertainty of such model would be treated the same way as here, thus likely causing only a biais on the final solution.

We sample the space of potential models without using any form of smoothing by using a Monte Carlo Markov Chain (MCMC) sampler based on the Cascading Adaptive Tempered Metropolis In Parallel algorithm (AlTar - Minson et al., 2013). The advantage of this approach is that it can handle any type of prior distribution. We adopt Laplacian prior distributions because they induce sparsity in the final solution, i.e., that the model parameters will tend to be non-zero only when required. In order to ensure a proper sampling of values around zero, we allow some negativity in the range of possible values explored by the sampler. Thus, for each parameter ϕ_{ij}, the prior laplacian distribution is bounded between -0.15 and 15.0 mm, peaks at 0.0, and has an exponential decay of 1.5. Consequently, the preslip model associated with the mode of the prior distributions is a zero-slip model.

3 Geodetic surface observations

3.1 Daily position time series

For the observations, we use surface displacements extracted from the daily position time series SOAM_GNSS_solENS (Klein et al., 2022). Raw GNSS data were processed following a double-difference approach using the GAMIT software (Herring et al., 2010a), combined with the GLOBK software (Herring et al., 2010b) and expressed in the ITRF2014 (Altamimi et al., 2016) using the PyACS software (https://github.com/JMNocquet/pyacs36). Then, we select the time series from the 23 closest stations located in Chile and operated by the Centro Sismologico Nacional (CSN, Báez et al., 2018, ,see Fig.1a). We choose to disregard the vertical component because of its higher noise level.

Using these position time series, we fit a trajectory model composed of : (1) piecewise linear functions, representing the inter-seismic velocity, and occasional offsets due to earthquakes, equipment changes or other unknown causes, (2) annual and semi-annual sine functions, representing the seasonal signals, and (3) exponential functions, representing post-seismic signals following large earthquakes. Once the parameters of that trajectory model are adjusted, we only remove the annual and semi-annual components. From these time series corrected from seasonal signals, we compute the inter-seismic trend by fitting a linear function using the positions from February 2011 to July 2013. The start date is chosen $\sim$1 year after the 2010 earthquake in Maule, Chile (magnitude 8.8) to avoid any potential contamination from the post-seismic signal of this event. The end date is chosen so that it stops before the $\sim$8 months long preparatory phase of the Iquique earthquake (Socquet et al., 2017). The obtained linear trend is then removed from the entire time series.

We consider only the 31 days that precede the mainshock. Because of the reported long initiation phase of the Iquique earthquake (Socquet et al., 2017), it is possible that our time series already exhibits some static displacement at the beginning, and which would be linked to the potential slip history occurring prior the time period of interest. To remove this effect, we remove a constant from the time series, which is estimated over a time window of 7 days preceding the period on which we focus our study. These are our observations for inferring the spatial and temporal evolution of preslip during the month prior to Iquique earthquake (Figure 2a).

To build the data covariance matrix ($\mathbf{C}_d$) for the inverse problem, we choose not to use the nominal errors provided by the processing software. Instead, using the position time series corrected for the seasonal signals, we compute the standard deviation of the time series over the inter-seismic period (i.e., from February 2011 to July 2013, a time period when there are no earthquakes larger than M_w6.5). Then, these values are used to fill the diagonal elements of $\mathbf{C}_d$. Off-diagonal elements are set to zero, making the assumption that each data point is independent. Over the inter-seismic period, the time series are likely affected by white and colored noise. Therefore, the values in $\mathbf{C}_d$ might not be representative of the noise level of 31-days long time series, this latter time window being mostly dominated by white noise (see Langbein, 2012). Indeed, when calculating the standard deviation over 31-days time-windows, we find that we could lower the values in the data covariance matrix by $\sim$30%. Yet, we choose the former estimates to be conservative regarding the uncertainty level of the time series. We have also analysed the spatiotemporal correlations of the noise and the common-modes to justify the fact that we do not account for off-diagonal elements in $\mathbf{C}_d$ (see Supplementary Materials S1 for a detailed discussion on the matter).

Note that throughout the rest of the text, these data will be referred to as the uncorrected position time series or uncorrected data.

4 Seismic/Aseismic slip partitioning

To estimate the partitioning between seismic and aseismic slip during the initiation phase of the Iquique earthquake, we perform two separate inversions for the spatial and temporal pattern of preslip. The first one uses the data recording the combined contribution of seismic and aseismic slip on the fault (i.e., the uncorrected data). For the second one, we use data that reflects only aseismic slip on the fault, i.e., data that are corrected from the contribution of the foreshocks. By comparing the results from both inversions, we infer the partitioning between seismic and aseismic slip during the month that precedes the Iquique earthquake.

4.1 Correcting for the contribution of foreshocks

As it stands, geodetic observations alone cannot be used to determine the partitioning between these two modes of slipping since they record the combined contribution of seismic and aseismic slip on the plate interface. To infer aseismic slip only, we need to account for the contribution that seismic slip from the foreshocks has on our surface observations. Thus, a methodology is designed to compute the surface displacements induced by the foreshocks at the stations while accounting for potential errors on the focal mechanism and hypocentral location. This is similar to the approach taken by (Bedford et al., 2015) with the exception that (1) we use the multi-layered media obtained by Husen et al. (1999) to compute the response of the foreshocks at the stations and (2) we use a finite-fault model for the largest foreshock.

We correct for foreshocks that are in the catalog of focal mechanisms obtained by Cesca et al. (2016), which includes all earthquakes with moment magnitude larger than 4.0. The contribution of smaller events can likely be neglected as pointed out for the 2017 Valparaiso earthquake sequence by Caballero et al. (2021).

Our approach consists of generating 50,000 synthetic earthquake catalogs by randomly sampling around the focal mechanisms, locations and moment magnitude given by the catalog ($\sigma_{\text{strike}} = 12°$, $\sigma_{\text{dip}} = 5°$, and $\sigma_{\text{rake}} = 9°$), the location ($\sigma_{\text{lat}} = 0.05°$, $\sigma_{\text{lon}} = 0.12°$, and $\sigma_{\text{depth}} = 5$ km). This is used to derive 50,000 synthetic time series of earthquake-induced surface displacements (Figure 2b). We subtract these synthetic time series to 50,000 position time series, sampled within the observation uncertainties assuming a Gaussian noise distribution (Figure 2c). These position time series are effectively samples of the displacement time series recording the aseismic part of slip along the megathrust during the precursory phase leading to the Iquique earthquake. Final positions and uncertainties are taken as the mean and standard deviation of the 50,000 corrected time series. Note that we account for the time of the foreshocks by removing only a partial contribution on the day of the earthquakes, determined based on their times of occurrence with respect to the nominal time of the position (11:59:59 for each day, while the full offset is removed on the subsequent days.

Among the foreshocks, there is a significant one that occurred on March 16, 2014 (M_w6.7), i.e., 16 days before the Iquique mainshock, and it is the largest foreshock of the whole sequence. It has the particularity of not being located on the plate interface but instead within the upper plate along a sub-vertical fault plane (Ruiz et al., 2019). For this largest foreshock, we account for the finiteness of the source by using the finite-fault slip distribution obtained by Ruiz et al. (2019). This time, a random realization of the co-seismic offsets is obtained by perturbing the strike, dip and rake of the causative fault plane (i.e., the steeply-dipping plane) as well as its position, all within the ranges given above.

Note that throughout the rest of the text, the data corrected from the contribution of the foreshocks will be referred to as corrected position time series or corrected data (Figure 2a).

4.2 Spatio-temporal evolution of the preslip

Figure 3a shows the spatial distribution of aseismic slip obtained from the inversion of the corrected data on the day before the mainshock. It is derived by computing the mode of the posterior probability density function for each parameter. The mode is chosen to ensure a proper representation of zero-slip. Indeed, as the explored parameter-space is bounded, the posterior probability density functions might be truncated when slip gets close to zero, potentially biasing the mean or median. It shows that aseismic slip essentially occurs within a single patch that is located off-shore of the city of Pisagua, Chile (station PSGA) with a peak slip amplitude of $\sim$60 mm. This patch also coincides spatially with the location of the future mainshock as well as that of the largest foreshock (M_w=6.7). We note that the spatial resolution that we have adopted cannot rule out the fact that slip could be more heterogeneous at a smaller scale. We estimate the final moment released by aseismic slip over 1 month prior to the Iquique earthquake to be 6.2 $\times$ 10^{19} Nm with an uncertainty level of 4.4$\%$ (i.e., M_w=7.1).

Figure 3b shows the temporal evolution of the moment-rate function for the mode-model as well as the family of models that we have obtained from the inversion. It shows that not much is happening between 31 and 20 days before the Iquique earthquake. Then, the moment-rate starts to accelerate, reaching its peak amplitude about 15 days prior to the mainshock.

It is during that acceleration stage that the largest foreshock occurs, and the peak amplitude of the moment-rate function coincides with the occurrence of a large number of earthquakes. After that, the moment-rate decelerates up to about 5 days before the future mainshock, a point when it accelerates again until the day before the Iquique earthquake. The fit to the observations can be seen in Supplementary Materials S2. Overall, the modeled surface displacements are in good agreement with the observations. However, on the east components of some stations, we find that the calculated surface displacements often exceed the observed ones. We believe that this is likely due to the fact that we fix the slip vector to be parallel to the convergence vector from the MORVEL model, and which might slightly differ from the actual slip direction.

As a point of comparison, we also show the results obtained using the uncorrected data (see Figure 3c and Figure 3d), which exhibits a very similar spatial and temporal pattern. One major difference is in the slip amplitude. Indeed, the moment on the day before the earthquake is about 8.3×10^{19} Nm with an uncertainty level of about 3.1% (i.e., $\mathrm{M_w}7.2$). This corresponds to a difference of 2.1×10^{19} Nm between the model obtained using the corrected data and the one obtained using the uncorrected data. This is consistent with the cumulative seismic moment released by the foreshocks with moment magnitude larger than 4.0 (i.e., 2.2×10^{19} Nm). Another major difference is in the temporal pattern, with the presence of a secondary peak in the moment-rate function around 10 days before the future mainshock and that coincides with the occurrence of a large number of foreshocks. Thus, that secondary peak is clearly associated to seismic slip as it disappears when using data corrected from the contribution of foreshocks.

4.3 Estimation of the Seismic/Aseismic slip partitioning

We estimate the seismic/aseismic slip partitioning by comparing the time evolution of slip from the two inversions. At each time step, we compute the percentage of aseismic slip on the fault using the following formula:

$$\mathrm{fraction_{aseismic}} = \frac{\mathrm{preslip_{corrected}}}{\mathrm{preslip_{uncorrected}}} \times 100 \tag{5}$$

$\mathrm{preslip_{uncorrected}}$ and $\mathrm{preslip_{corrected}}$ correspond to the preslip integrated over the whole fault and obtained using the uncorrected and corrected data respectively. We find that once significant slip starts to occur (i.e., from 20 days prior to the mainshock), uncertainty on $\mathrm{fraction_{aseismic}}$ drops significantly, and the percentage of aseismic slip stabilizes around 80% with a variation of $\pm$ 3% (see Figure 4a).

When we compare our estimate for the percentage of aseismic slip with other studies, we find that our estimate is significantly larger than those obtained by others. For instance, Socquet et al. (2017) estimates that after the largest foreshock, which occurs 15 days before the Iquique earthquake, aseismic slip accounts for 33 to 35 % of the slip on the fault inferred from the geodetic observations. Meanwhile, Kato et al. (2016) find that during the month preceding the Iquique earthquake aseismic slip accounts for about 50% of the total slip that can be inferred from the surface observations. The differences between these estimates and ours could partly be explained by the fact that different velocity models are used between the different studies (CRUST1.0 for Socquet et al. 2017, and a homogeneous half-space for Kato et al. 2016). Indeed, our velocity model have rigidities at the depths where slip occurs that are about 1.3 times larger than that of CRUST1.0 and the value used by Kato et al. (2016) In addition, our estimation of the seismic/aseismic slip partitioning is done over the entire fault. Instead, if we focus on the region with the largest aseismic slip amplitude (blue dashed line on Figure 4b), we find that aseismic slip rather represents about 60% with a variation of $\pm$ 3%.

In addition, Kato et al. (2016) also provide the time evolution of aseismic slip inferred from the study of repeating earthquakes. After converting the seismic moment of the repeating earthquakes into aseismic slip on the fault thanks to a standard scaling relationship, they average the aseismic slip inferred for each family of repeating earthquakes to obtain the characteristic time evolution of aseismic slip in the vicinity of the future mainshock (red dashed line on Figure 5). When we compare this independent estimate of the time evolution of aseismic slip with our estimate (red and gray lines on Figure 5), we find a relatively good agreement, the estimates from Kato et al. (2016) being within the level of uncertainty of the results from our study.

5 The physical origin of the aseismic slip

5.1 The main phase of aseismic slip

Several hypothesis have been drawn as to what is the physical origin of aseismic slip observed over the month preceding the Iquique earthquake. It has been suggested that it is essentially a slow-slip event (e.g., Ruiz et al., 2014). This is expected in the slow-slip model for earthquake nucleation, a behavior often observed in laboratory experiments (e.g., Latour et al., 2013). Some have instead proposed that it is essentially afterslip from the intense foreshocks sequence prior to the future mainshock (e.g., Bedford et al., 2015). Finally, it is also possible that both processes are occurring at the same time (e.g., Socquet et al., 2017), either within the same patch, or over two spatially distinct regions. However, this is a level of spatial heterogeneity that we cannot access given the parametrization that we have adopted here. Thus, we can only infer the large scale behavior of the slipping patch imaged by the inversion. Based on our results, we have several reasons to believe that afterslip is not the primary mechanism of the aseismic slip that is observed.

The first argument is based on a comparison between the moment released by aseismic slip and the moment released by seismic slip from the foreshocks. Our results shows that the moment of aseismic slip is about 2.8 times the seismic moment released by the foreshocks from the earthquake catalog of Cesca et al. (2016). This leads to a post-seismic to co-seismic moment ratio that is excessively large. For instance, Hawthorne et al. (2016) estimate that this ratio ranges between 0.5 to 1.5 (based on earthquakes with moment magnitude between 1.9 and 5.0 from California). This has been recently refined by Alwahedi and Hawthorne (2019) for earthquakes with moment magnitude from 4.0 and 5.0. They find that the post-seismic to co-seismic moment ratio is about 0.45, with a 90% confidence interval between 0.25 and 0.60. Therefore, we can estimate the moment released by afterslip to be around 1.0×10^{19} Nm, which is only about 15 to 20 % of the overall moment that we obtain from the corrected data. This can go up to $\sim$50 % if we focus on the region where most of the aseismic slip occurs (blue dashed line on Figure 3c), and that has a moment of 2.0×10^{19} Nm. Therefore, even accounting for afterslip, a significant portion of aseismic slip would remain.

The second argument is based on the fact that aseismic slip begins prior to the start of the foreshocks sequence. Figure 6 shows the spatial and temporal evolution of aseismic slip along with that of the foreshocks from the earthquake catalog of

Cesca et al. (2016). We see that slip-rate begins to accelerate 19 days before the occurrence of the Iquique earthquake, which is 3 days before the occurrence of the largest foreshock of the sequence. This time window is resolved by two basis functions starting before the largest foreshock. Such backward leakage of afterslip is unlikely given that our inversion scheme does not include temporal smoothing. Also, the 3 days time window before the March 16 foreshock, when slip starts to occur, is longer than the temporal spacing between two consecutive basis functions.

The final argument is on the size and duration of that aseismic slip phase. If we focus on the time period where the moment-rate exceeds its standard deviation and on the region where most aseismic slip occurs, we find that the main aseismic slip phase lasts for about 10 days with a moment of 2.0×10^{19} Nm. This gives a moment and duration for this event that are comparable with what has been reported for other slow-slip events in the literature (e.g., Ide et al., 2007; Michel et al., 2019).

However, Boudin et al. (2019) argue that adding to the GNSS data a tilt records from Santa Rose, Chile ($\sim$8 km north-east of the station IQQE) changes the spatio-temporal resolution in such a way that it rules out the occurrence of a slow-slip event with magnitude larger than 6.6 near the epicenter of the future mainshock. Instead, adding the tilt records suggests that the slow-slip activity occurs more to the south (around 20.5°S) compared to what we have identified in this study (around 20.0°S). To test the sensitivity of the tilt records with respect to the slow-slip event from this study, we have computed the amount of tilt generated by the family of models for our slow-slip event (see Supplementary Materials S3). The main difference with Boudin et al. (2019) is that the computation of the tilt is done using a layered velocity model for the region, the same that we have used to obtain our models. Our findings suggest that the final amplitude of the tilt generated by the slow-slip event from this study barely exceeds the noise level reported by Boudin et al. (2019) – 48 and 42 nrad for the north and east components, respectively. Thus, it is possible that adding the tilt records bias the resolution towards the region near the tilt meter, allowing the identification of additional slow-slip events, but missing the one near the epicenter of the Iquique earthquake because of the small signal it generates at the tilt meter when compared to the noise level.

Therefore, rather than afterslip, this first phase of aseismic slip seems more consistent with a slow-slip event. But, unlike the proposed slow-slip model for earthquake nucleation, this episode is not self-accelerating up to the future mainshock but instead ends about 7 to 6 days prior to the Iquique earthquake. Because the slow-slip event starts to decelerate about 2 days after the occurrence of the largest foreshock, we investigate the impact of this foreshock on the on-going aseismic slow slip. Because this foreshock is an oblique thrust faulting event that ruptured in the forearc material above the megathrust, it is reasonable to hypothesis that some portions of the megathrust should experience significant normal stress changes from that earthquake. To verify that, using the finite-fault slip model from Ruiz et al. (2019), we compute the Coulomb static stress change on the subduction interface induced by this foreshock (Figure 7). We find that the pattern of static Coulomb stress change is complex with regions experiencing stress increase and regions experiencing stress decrease. However, the core region of the slow-slip event exhibits a significant stress decrease, suggesting that the largest foreshock might have contributed to the deceleration of the slow-slip event. Herman et al. (2016), have attempted a more complete assessment of the static stress change evolution throughout the entire foreshock sequence. The comparison between their results and our aseismic preslip model leads to the same conclusion that the core region of the slow-slip event experiences a significant stress decrease even when considering the full foreshock sequence. Thus, the foreshocks sequence could have contributed, if not induced, the slow down of the slow-slip event.

5.2 Aseismic slip just prior to the Iquique earthquake

As mentioned previously, the moment-rate function for aseismic slip, when integrated over the entire fault plane, exhibits a significant increase starting about 5 days before the impending mainshock (see Figure 3b). But, the spatio-temporal evolution of the slip-rate over these last few days shows no clear spatial signature of that increase (see Figure 6). Instead, during this time period, slip-rate seems to accelerate just mildly across the entire fault interface.

To find out if that final stage is reliable, we compute a measure of scale to quantify the statistical dispersion of the posterior probability density functions. This is done by computing the modified coefficient of variation, i.e., the difference between the third and first quartile that we divide by the mode of the posterior probability density functions (see Figure 8). Values less than 1 are associated with very narrow distributions, narrower than the mode value itself, highlighting very well constrained parameters. Instead, values greater than 1 suggest a significant dispersion of the posterior probability density functions, thus highlighting parameters with large uncertainties, the dispersion being larger than the inferred value itself.

First, we find that during the main episode of aseismic slip, the modified coefficient of variation is well below 1.0 where slip-rate is found to be large (see Figure 6). This means that the slow-slip event that we identify is well resolved. Instead, during the few days preceding the future mainshock, the modified coefficient of variation is higher and fluctuates around 1.0. For the last day, it is even larger than 1.0 over the entire fault. Therefore, the few days preceding the future mainshock are associated to a large level of uncertainty.

This questions the reliability of the late acceleration phase of the moment-rate function observed just prior to the Iquique earthquake(see Figure3b). In fact, if we focus on the 2 nodes experiencing the largest slip-rate amplitudes (see labels A and B on Figure 8) and that are also close to the future epicenter of the Iquique earthquake, we do not observe any significant increase of the moment-rate at the very end (Figure 9). With this caveats in mind, we cannot completely rule out the possibility of a self-accelerating slow-slip episode just before the Iquique earthquake. There might be a small signal that the inversion cannot resolve spatially but that comes apparent when integrating the time evolution over the entire fault.

6 Conclusions

In this study, we have analyzed the initiation phase of the 2014 Iquique, Chile, earthquake ($M_w = 8.1$). To that end, we have developed a Bayesian inversion scheme to infer how the preslip evolves in space and time while providing an estimation of the associated uncertainty. Our goal are two-folds : (1) estimate more accurately the partitioning between seismic and aseismic slip over the month that precedes the future mainshock and (2) use the spatio-temporal evolution to infer the physical origin of the aseismic slip prior to the Iquique earthquake.

We find that most of the slip ($80\% \pm 3\%$) is in fact aseismic slip (60% if we focus on the region where most aseismic slip occurs), the remaining part being imputed to the seismic activity that occurs prior to the mainshock. The aseismic slip is likely a slow-slip event that starts about 19 days before the April 1, mainshock and stops 7 to 6 days prior to it. Although we have clear evidences for the presence of a slow-slip event during the initiation phase of the Iquique earthquake, it does not exhibit the self-accelerating behavior expected from the slow-slip model for earthquake nucleation. From an analysis of the static Coulomb stress changes, we find that the largest foreshock might have contributed to slow-down the slow-slip event.

We also find that when we integrate the aseismic slip history over the entire fault that the time evolution exhibits a final stage of the slip-rate acceleration only a few days prior to the future mainshock. However, this last stage shows large uncertainties and cannot be resolved spatially.

To conclude, our study suggests that the initiation phase of the Iquique earthquake might be more consistent with a hybrid model for earthquake nucleation, with the coexistence of an intense seismic activity and a slow-slip event, both phenomenon potentially interacting : the slow-slip event triggering the foreshock sequence and the foreshock sequence potentially shutting down the slow-slip event.

Acknowledgements. This work was supported by the European Research Council under the European's Union Horizon 2020 research and innovation program (grant numbers 805256 and 758210). It also benefited from the support of the Agence National de la Recherche (grant number ANR-19-CE31-0003). The authors are thankful to the CSN for providing the data used in this study. The authors would also like to thanks Simone Cesca for providing the catalog of focal mechanisms from his 2016's article as well as Javier Ruiz for providing the finite fault slip model from his 2019's article. The authors thank Christophe Vigny for providing feedback throughout the course of the study, as well as Emmanuel Caballero and Luc Moutote for fruitful discussions regarding the interpretation of the results. We also thank the editor for handling the manuscript, and two anonymous reviewers for providing suggestions that substantially improved the manuscript.

References

Altamimi, Z., Rebischung, P., Métivier, L., and Collilieux, X.: ITRF2014: A new release of the International Terrestrial Reference Frame modeling nonlinear station motions, J. Geophys. Res. Solid Earth, 121, 6109–6131, https://doi.org/10.1002/2016JB013098, 2016.

Alwahedi, M. A. and Hawthorne, J. C.: Intermediate-Magnitude Postseismic Slip Follows Intermediate-Magnitude (M 4 to 5) Earthquakes in California, Geophys. Res. Lett., 46, 3676–3687, https://doi.org/10.1029/2018GL081001, 2019.

Báez, J. C., Leyton, F., Troncoso, C., del Campo, F., Bevis, M., Vigny, C., Moreno, M., Simons, M., Kendrick, E., Parra, H., and Blume, F.: The Chilean GNSS Network: Current Status and Progress toward Early Warning Applications, Seism. Res. Lett., 89, 1546–1554, https://doi.org/10.1785/0220180011, 2018.

Bedford, J., Moreno, M., Schurr, B., Bartsch, M., and Oncken, O.: Investigating the final seismic swarm before the Iquique-Pisagua 2014 Mw8.1 by comparison of continuous GPS and seismic foreshock data, Geophys. Res. Lett., 42, 3820–3828, https://doi.org/10.1002/2015GL063953, 2015.

Bird, P.: An updated digital model of plate boundaries, Geochem. Geophys. Geosyst., 4, 1027, https://doi.org/10.1029/2001GC000252, 1993.

Boudin, F., Bernard, P., Meneses, G., Vigny, C., Olcay, M., Tassara, C., Boy, J. P., Aissaoui, E., Metois, M., Satriano, C., Esnoult, M.-F., Nercessian, A., Vallee, M., Vilotte, J.-P., and Brunet, C.: Slow slip events precursory to the 2014 Iquique Earthquake, revisited with long-base tilt and GPS records, Geophys. J. Int., accepted, https://doi.org/10.1093/gji/ggab425, 2019.

Brune, J. N.: Implications of earthquake triggering and rupture propagation for earthquake prediction based on premonitory phenomena, J. Geophys. Res., 84, 2195–2198, https://doi.org/10.1029/JB084iB05p02195, 1979.

Caballero, E., Chounet, A., Duputel, Z., Jara, J., Twardzik, C., and Jolivet, R.: Seismic and aseismic fault slip during the initiation phase of the 2017 Mw=6.9 Valparaíso earthquake, Geophys. Res. Lett., 48, e2020GL091 916, https://doi.org/10.1029/2020GL091916, 2021.

Cesca, S., Grigoli, F., Heimann, S., Dahm, T., Kriegerowski, M., Sobiesak, M., Tassara, C., and Olcay, M.: The M_w8.1 2014 Iquique, Chile, seismic sequence: a tale of foreshocks and aftershocks, Geophys. J. Int., 204, 1766–1780, https://doi.org/10.1093/gji/ggv544, 2016.

Comte, D. and Pardo, M.: Reappraisal of great historical earthquakes in the northern Chile and southern Peru seismic gaps, Nat. Hazards, 4, 23–44, https://doi.org/10.1007/BF00126557, 1991.

DeMets, C., Gordon, R., and Argus, D.: Geologically current plate motions, Geophys. J. Int., 181, 1–80, https://doi.org/10.1111/j.1365-246X.2009.04491.x, 2010.

Duputel, Z., Agram, P. S., Simons, M., Minson, S. E., and Beck, J. L.: Accounting for prediction uncertainty when inferring subsurface fault slip, Geophys. J. Int., 197, 464–482, https://doi.org/10.1093/gji/ggt517, 2014.

Duputel, Z., Jiang, J., Jolivet, R., Simons, M., Rivera, L., Ampuero, J.-P., Riel, B., Owen, S. E., Moore, A. W., Samsonov, S. V., Culaciati, F. O., and Minson, S. E.: The Iquique earthquake sequence of April 2014: Bayesian modeling accounting for prediction uncertainty, Geophys. Res. Lett., 42, 7949–7957, https://doi.org/10.1002/2015GL065402, 2015.

Ellsworth, W. L. and Beroza, G. C.: Seismic evidence for an earthquake nucleation phase, Science, 268, 851–855, https://doi.org/10.1126/science.268.5212.851, 1995.

Ellsworth, W. L. and Bulut, F.: Nucleation of the 1999 Izmit earthquake by a triggered cascade of foreshocks, Nature Geosci., 11, 531–535, https://doi.org/10.1038/s41561-018-0145-1, 2018.

Gomberg, J.: Unsettled earthquake nucleation, Nature Geosci., 11, 463–464, https://doi.org/10.1038/s41561-018-0149-x, 2018.

Hawthorne, J. C., Simons, M., and Ampuero, J.-P.: Estimates of aseismic slip associated with small earthquakes near San Juan Bautista, CA, J. Geophys. Res. Solid Earth, 121, 8254–8275, https://doi.org/10.1002/2016JB013120, 2016.

Hayes, G. P., Moore, G. L., Portner, D. E., Hearne, M., Flamme, H., Furtney, M., and Smoczyk, G. M.: Slab2, a comprehensive subduction zone geometry model, Science, 362, 58–61, https://doi.org/10.1126/science.aat4723, 2018.

Herman, M. W., Furlong, K. P., Hayes, G. P., and Benz, H. M.: Foreshock triggering of the 1 April 2014 Mw 8.2 Iquique, Chile, earthquake, Earth Planet. Sci. Lett., 447, https://doi.org/10.1016/j.epsl.2016.04.020, 2016.

Herring, T., King, R., and McClusky, S. C.: GAMIT : GPS analysis at MIT, release 10.4, 2010a.

Herring, T., King, R., and McClusky, S. C.: GLOBK : Global Kalman filter VLBI and GPS analysis program release 10.4, 2010b.

Husen, S., Kissling, E., Flueh, E., and Asch, G.: Accurate hypocentre determination in the seismogenic zone of the subducting Nazca plate in northern Chile using a combined on-/offshore network, Geophys. J. Int., 138, 687–701, https://doi.org/10.1046/j.1365-246x.1999.00893.x, 1999.

Ide, S., Beroza, G. C., Shelly, D. R., and Uchide, T.: A scaling law for slow earthquakes, Nature, 447, 76–79, https://doi.org/10.1038/nature05780, 2007.

Iio, Y.: Observations of the slow initial phase generated by microearthquakes: Implications for earthquake nucleation and propagation, J. Geophys. Res., 100, 15 333–15 349, https://doi.org/10.1029/95JB01150, 1995.

Kato, A., Fukuda, J., Kumazawa, T., and Nakagawa, S.: Accelerated nucleation of the 2014 Iquique, Chile Mw8.2 earthquake, Sci. Rep., 6, 24 792, https://doi.org/10.1038/srep24792, 2016.

Klein, E., Vigny, C., Nocquet, J.-M., and Boulze, H.: A 20 year-long GNSS solution across South-America with focus in Chile, BSGF - Earth Sci. Bull., accepted, 2022.

Langbein, J.: Estimating rate uncertainty with maximum likelihood: differences between power-law and flicker-random-walk models, J. Geod., 86, 775–783, https://doi.org/10.1007/s00190-012-0556-5, 2012.

Laske, G., Masters, G., Ma, Z., and Pasyanos, M.: Update on CRUST1.0 - A 1-degree global model of Earth's crust, Geophys. Res. Abstracts, 15, Abstract EGU2013–2658, 2013.

Latour, S., Schubnel, A., Nielsen, S., Madariaga, R., and Vinciguerra, S.: Characterization of nucleation during laboratory earthquakes, Geophys. Res. Lett., 40, 5064–5069, https://doi.org/10.1002/grl.50974, 2013.

Legrand, D., Delouis, B., Dorbath, L., David, C., Campos, J., Marquéz, L., Thompson, J., and Comte, D.: Source parameters of the Mw=6.3 Aroma crustal earthquake of July 24, 2001 (northern Chile), and its aftershock sequence, J. South Amer. Earth Sci., 24, 58–68, https://doi.org/10.1016/j.jsames.2007.02.004, 2007.

Lüth, S.: Results of wide-angle investigations and crustal structure along a traverse across the central Andes at 21 degrees south, Ph.D. thesis, Berliner Geowissenschaftliche Abhandlungen, Inst. of Geol., Geophys. and Geoinformatics, Free Univ. of Berlin, Berlin, 2000.

Masterlark, T.: Finite element model predictions of static deformation from dislocation sources in a subduction zone: Sensitivities to homogeneous, isotropic, Poisson-solid, and half-space assumptions, J. Geophys. Res. Solid Earth, 108, 2540, https://doi.org/10.1029/2002JB002296, 2003.

McLaskey, G. C.: Earthquake Initiation From Laboratory Observations and Implications for Foreshocks, J. Geophys. Res. Solid Earth, 124, 12 882–12 904, https://doi.org/10.1029/2019JB018363, 2019.

Meng, L., Huang, H., Bürgmann, R., Ampuero, J. P., and Strader, A.: Dual megathrust slip behaviors of the 2014 Iquique earthquake sequence, Earth Planet. Sci. Lett., 411, 177–187, https://doi.org/10.1016/j.epsl.2014.11.041, 2015.

Métois, M., Socquet, A., Vigny, C., Carrizo, D., Peyrat, S., Delorme, A., Maureira, E., Valderas-Bermejo, M.-C., and Ortega, I.: Revisiting the North Chile seismic gap segmentation using GPS-derived interseismic coupling, Geophys. J. Int., 194, 1283–1294, https://doi.org/10.1093/gji/ggt183, 2013.

Michel, S., Gualandi, A., and Avouac, J.-P.: Similar scaling laws for earthquakes and Cascadia slow-slip events, Nature, 574, 522–526, https://doi.org/10.1038/s41586-019-1673-6, 2019.

Minson, S. E., Simons, M., and Beck, J. L.: Bayesian inversion for finite fault earthquake source models I-theory and algorithm, Geophys. J. Int., 194, 1701–1726, https://doi.org/10.1093/gji/ggt180, 2013.

Ohnaka, M.: Earthquake source nucleation: A physical model for short-term precursors, Tectonophysics, 211, 149–178, https://doi.org/10.1016/0040-1951(92)90057-D, 1992.

Olson, A. H. and Aspel, R. J.: Finite faults and inverse theory with applications to the 1979 Imperial Valley earthquake, Bull. Seism. Soc. Am., 72, 1969–2001, 1982.

Porta, J., Verbeek, J., and Kröse, B.: Active Appearance-Based Robot Localization using Stereo Vision, Auton. Robot., 18, 59–80, https://doi.org/10.1023/B:AURO.0000047287.00119.b6, 2005.

Ruiz, J. A., Maksymowicz, A., Ortega-Culaciatia, F., Rivera, L., and Comte, D.: Source characteristics of the March 16, 2014 M_w 6.7 earthquake and its implications for the M_w 8.2 Pisagua mainshock, Tectonophysics, 767, 687–701, https://doi.org/10.1016/j.tecto.2019.228170, 2019.

Ruiz, S., Métois, M., Fuenzalida, A., Ruiz, J., Leyton, F., Grandin, R., Vigny, C., Madariaga, R., and Campos, J.: Intense foreshocks and a slow slip event preceded the 2014 Iquique Mw 8.1 earthquake, Science, 345, 1165–1169, https://doi.org/10.1126/science.1256074, 2014.

Schurr, B., Asch, G., Hainzl, S., Bedford, J., Hoechner, A., Palo, M., Wang, R., Moreno, M., Bartsch, M., Zhang, Y., Oncken, O., Tilmann, F., Dahm, T., Victor, P., Barrientos, S., and Vilotte, J.-P.: Gradual unlocking of plate boundary controlled initiation of the 2014 Iquique earthquake, Nature, 512, 299–302, https://doi.org/10.1038/nature13681, 2014.

Socquet, A., na Valdes, J. P., Jara, J., Cotton, F., Walpersdorf, A., Cotte, N., Specht, S., Ortega-Culaciati, F., Carrizo, D., and Norabuena, E.: An 8-month slow slip event triggers progressive nucleation of the 2014 Chile megathrust, Geophys. Res. Lett., 44, 4046–4053, https://doi.org/10.1002/2017GL073023, 2017.

Tape, C., Holtkamp, S., Silwal, V., Hawthorne, J., Kaneko, Y., Ampuero, J. P., Ji, C., Ruppert, N., Smith, K., and West, M. E.: Earthquake nucleation and fault slip complexity in the lower crust of central Alaska, Nature Geosci., 11, 536–541, https://doi.org/10.1038/s41561-018-0144-2, 2018.

Williamson, A. L. and Newman, A. V.: Limitations of the resolvability of finite-fault models using static land-based geodesy and open-ocean tsunami waveforms, J. Geophys. Res. Solid Earth, 123, 9033–9048, https://doi.org/10.1029/2018JB016091, 2018.

Zhu, L. and Rivera, L. A.: A note on the dynamic and static displacements from a point source in multilayered media, Geophys. J. Int., 148, 619–627, https://doi.org/10.1046/j.1365-246X.2002.01610.x, 2012.

Figures

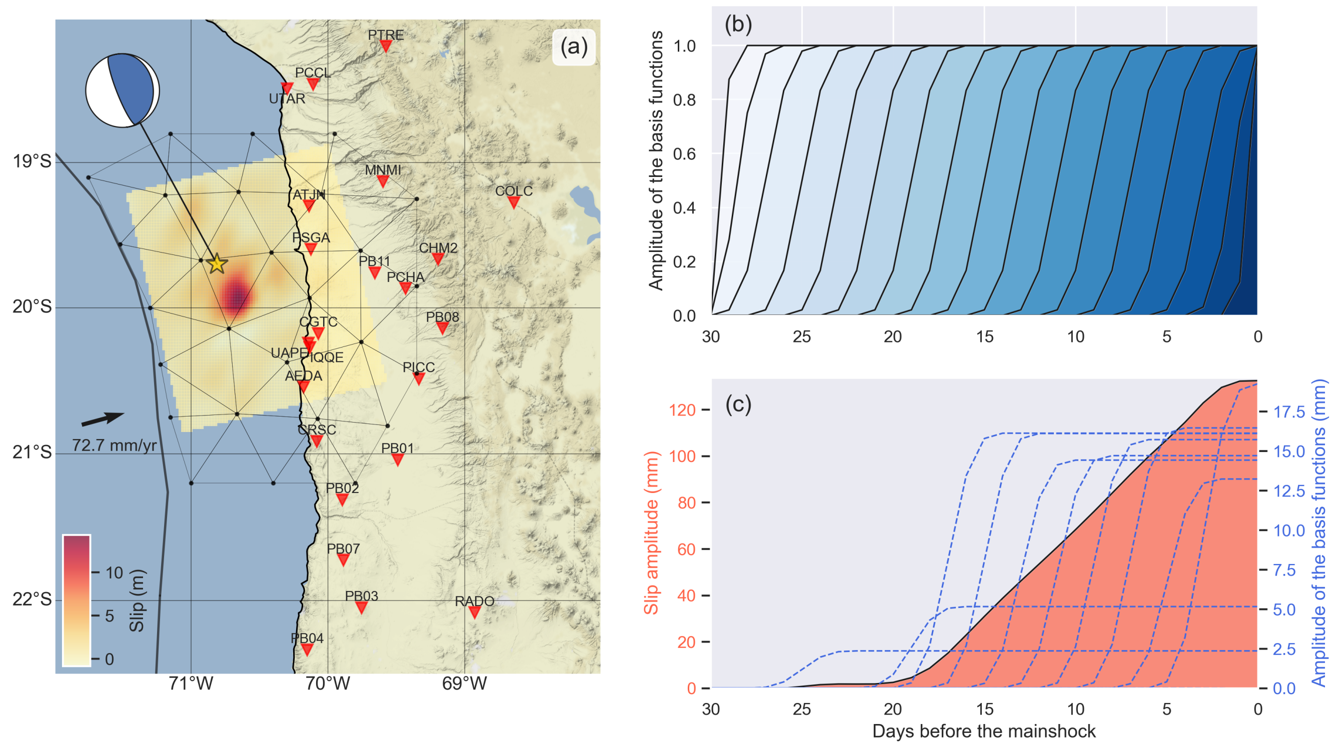

Figure 1. (a) Context map of the studied area. The yellow star shows the epicenter of the April 1, 2014, Iquique (Chile), earthquake (M_w8.1) along with its focal mechanism taken from the United States Geological Survey (USGS). We also show its slip distribution obtained by Duputel et al. (2015). The red triangles show the stations that we use to infer the spatio-temporal evolution of the preslip over the 1 month preceding the Iquique earthquake. Spatially, the preslip history is inferred on the nodes of the triangular mesh shown here. The mesh reproduces the geometry of the subducting plate given by the Slab2.0 model (Hayes et al., 2018). The thick black line outlines the trench from Bird (1993) and we show with the arrow the convergence vector between a fixed South American plate and the Nazca Plate from the MORVEL model (DeMets et al., 2010). (b) Set of basis functions that we use to infer the temporal evolution of the preslip at each node. (c) Example on how we model the temporal evolution of preslip at a given node. As illustrated by the blue dashed line, each basis function is scaled by a given coefficient (ϕ_{ij}, where i is the index of the node and j the index of the basis function). Once scaled, the basis functions are summed to give the temporal evolution of the preslip (red curve).

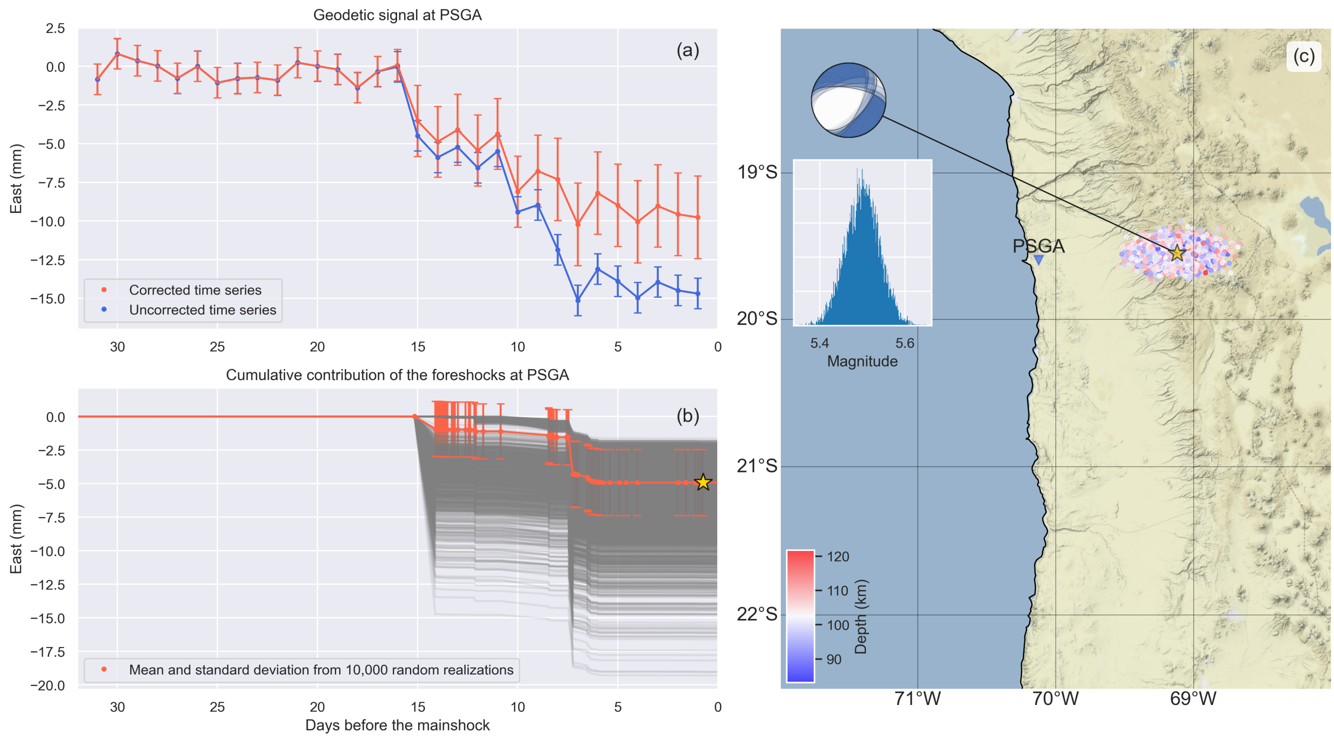

Figure 2. (a) East component of the position time series over the 1 month preceding the Iquique earthquake at station PSGA, identified on Figure 2c. The blue curve shows the uncorrected time series. The vertical bars show the errors on the position set as the standard deviation of the time series prior to period of interest. The red curve shows the corrected time series. (b) The grey lines show the contribution from 10,000 random realizations of the focal mechanisms for each foreshock to compute the respective static offsets on the east component at PSGA, and the red line shows the mean of the 10,000 random realizations, along with the standard deviation (vertical red bars). (c) Map illustrating for a given foreshock (yellow star on (b) and (c)) the range used for the 10,000 random realizations. The colored dots shows the variability of the hypocenter location, the color representing the depth. We show in the top-left corner the variability on the focal mechanism and in the bottom-left corner the variability on the magnitude.

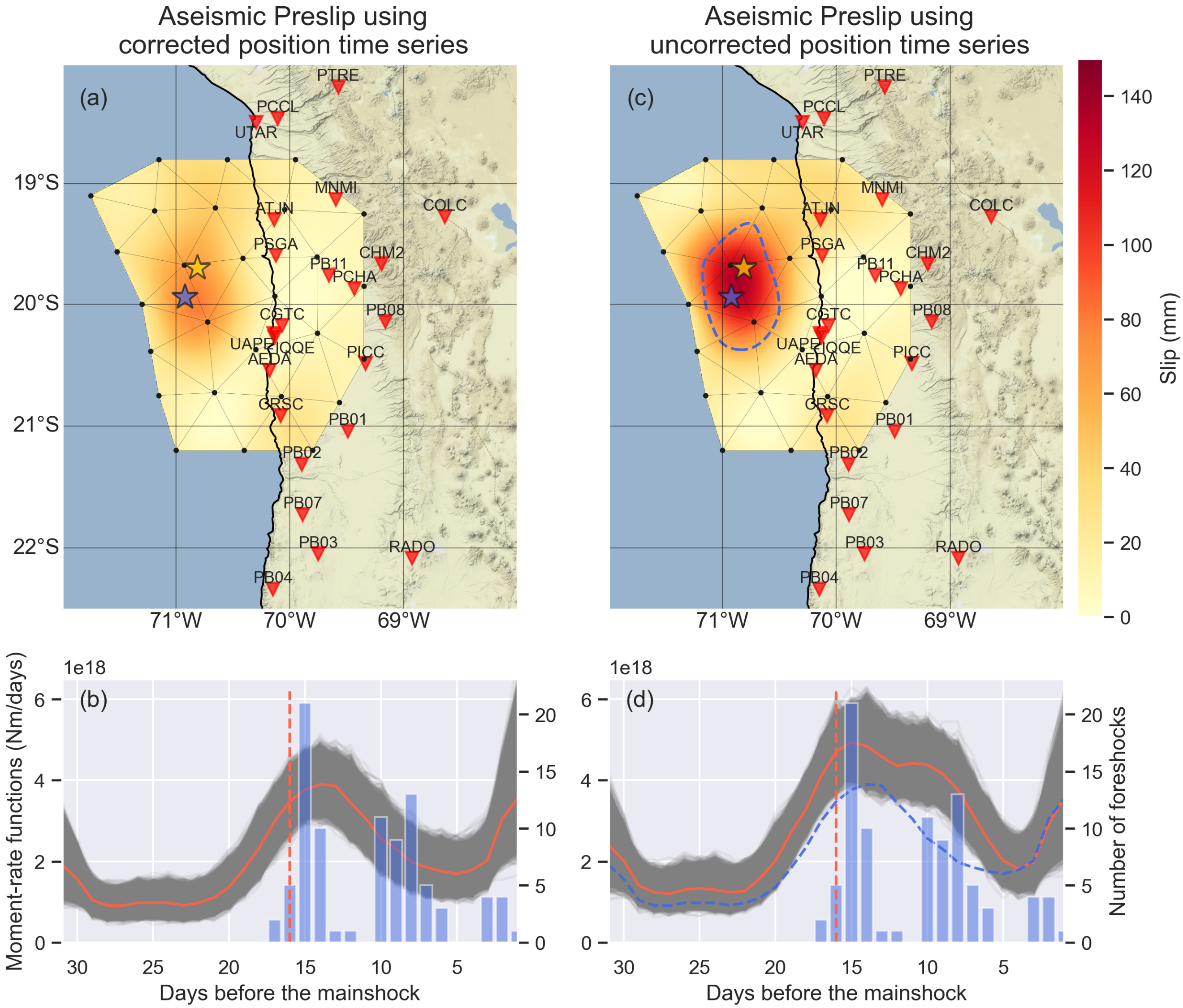

Figure 3. (a) Map showing the distribution of aseismic preslip obtained using the corrected position time series on the day before the April 1, 2014 Iquique earthquake. The preslip model shown here is obtained by computing the mode of the posterior probability density functions for each parameters. The red triangles show the station while the blue and yellow stars show the epicenter of the largest (M_w6.7) foreshock and of the mainshock, respectively. (b) Time evolution of the moment-rate. The grey lines show a selection of samples from the posterior probability density functions while the red line shows the mode of the posterior probability density functions. The vertical bars show the number of foreshocks during the month prior to the Iquique earthquake (right axis). We highlight with a red dashed line the day when the largest foreshock occurs. (c) Same as (a) except that it shows the preslip obtained using the uncorrected position time series, i.e., that it combines seismic and aseismic slip. For comparison, we also show with a blue dashed line the 50mm contour of the preslip model obtained using the corrected data. (d) Same as (b) except that it show the moment-rate for the models obtained using the uncorrected position time series. For comparison, we also show with a blue dashed line the time evolution of the moment-rate for the preslip model obtained using the corrected data.

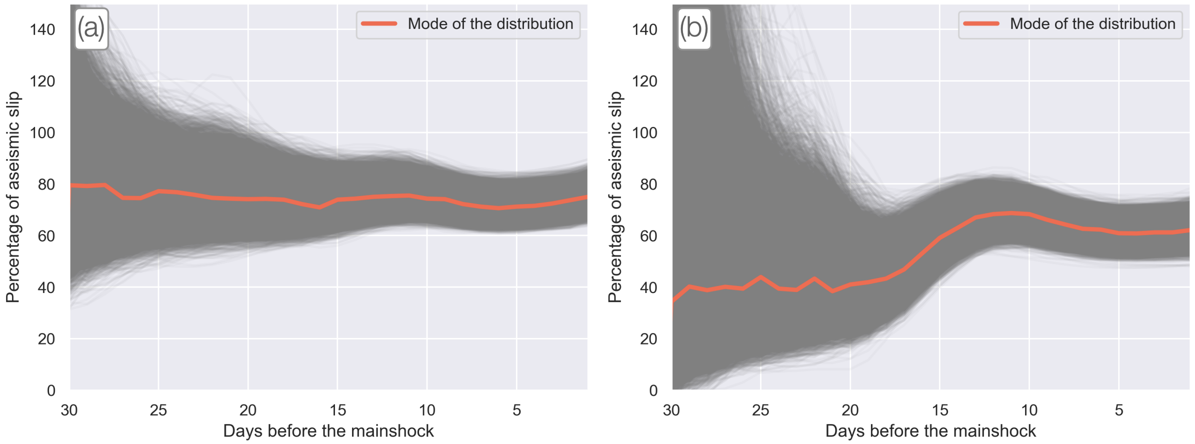

Figure 4. (a) Time evolution of the percentage of aseismic slip. The grey lines show a selection of samples from the posterior probability density functions while the red line is the mode of the posterior probability density functions. The percentage of aseismic slip is calculated using equation 5. (b) Same as (a) except that it shows the percentage of aseismic slip only for the two nodes that slip the most (red and blue dots on Figure 9).

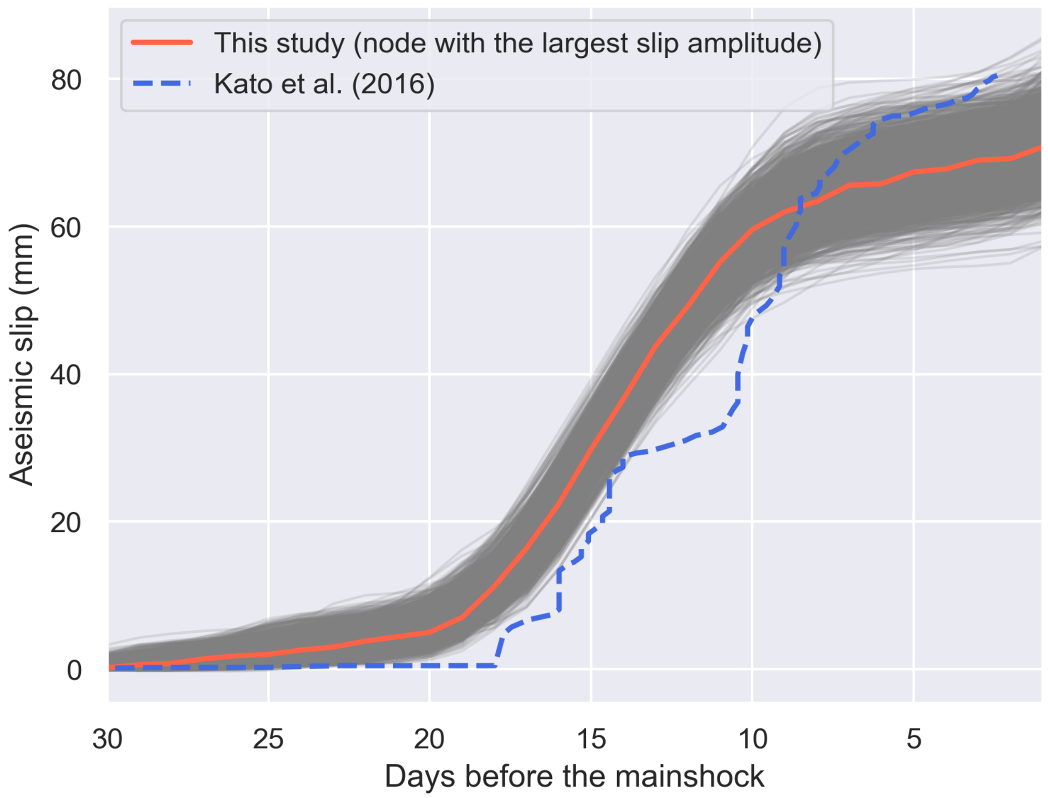

Figure 5. Comparison between the time evolution of aseismic slip from (Kato et al., 2016, , dashed line) and that from our study (plain line). The grey lines show a selection of samples for the time evolution of aseismic preslip.

.

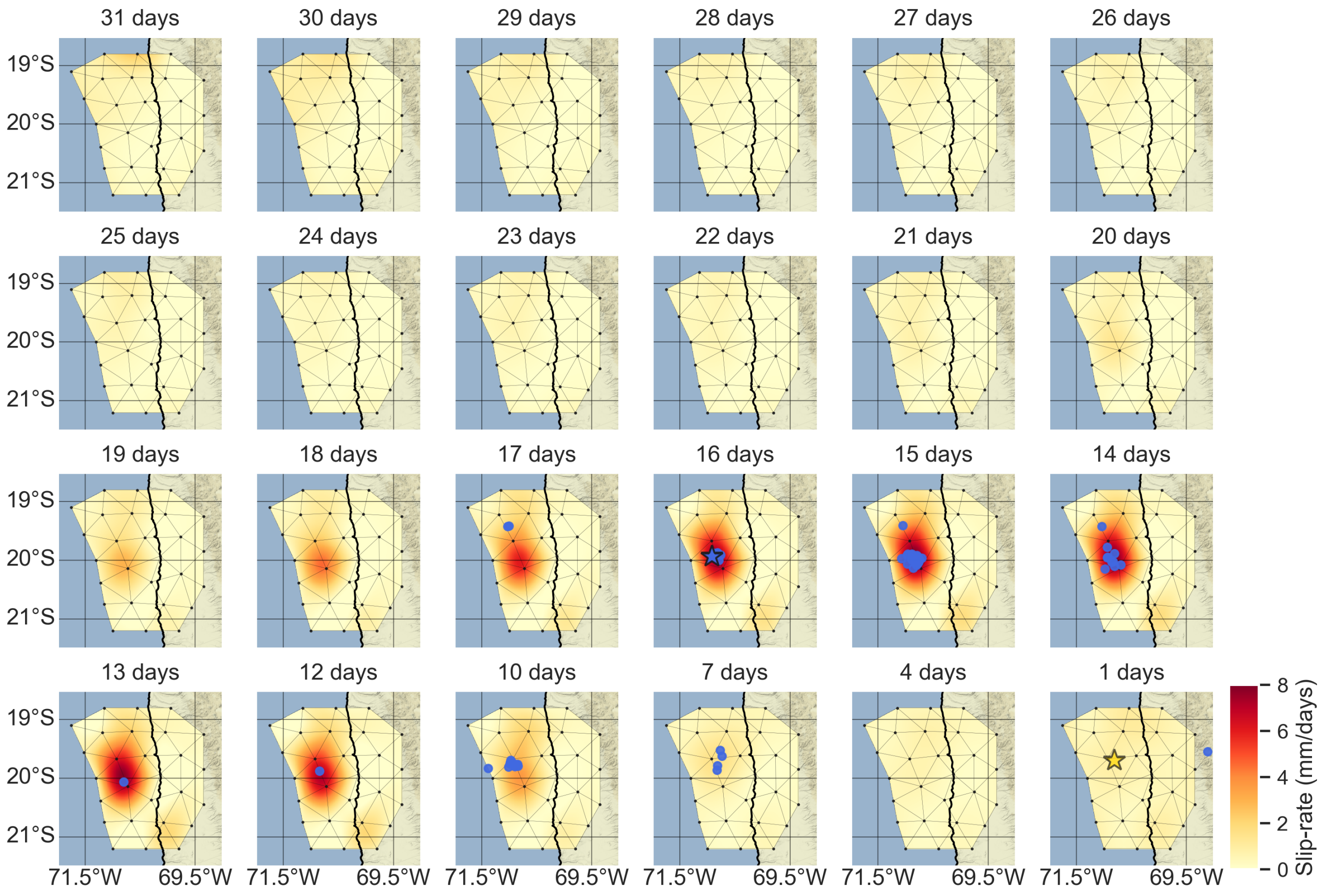

Figure 6. Spatial and temporal evolution of the aseismic slip-rate over the month that precedes the 2014 Iquique earthquake. The blue dots show the foreshocks over that same time period from the earthquake catalog from Cesca et al. (2016). We highlight with a yellow star the epicenter of the future mainshock and with a blue star the largest foreshock of the sequence.

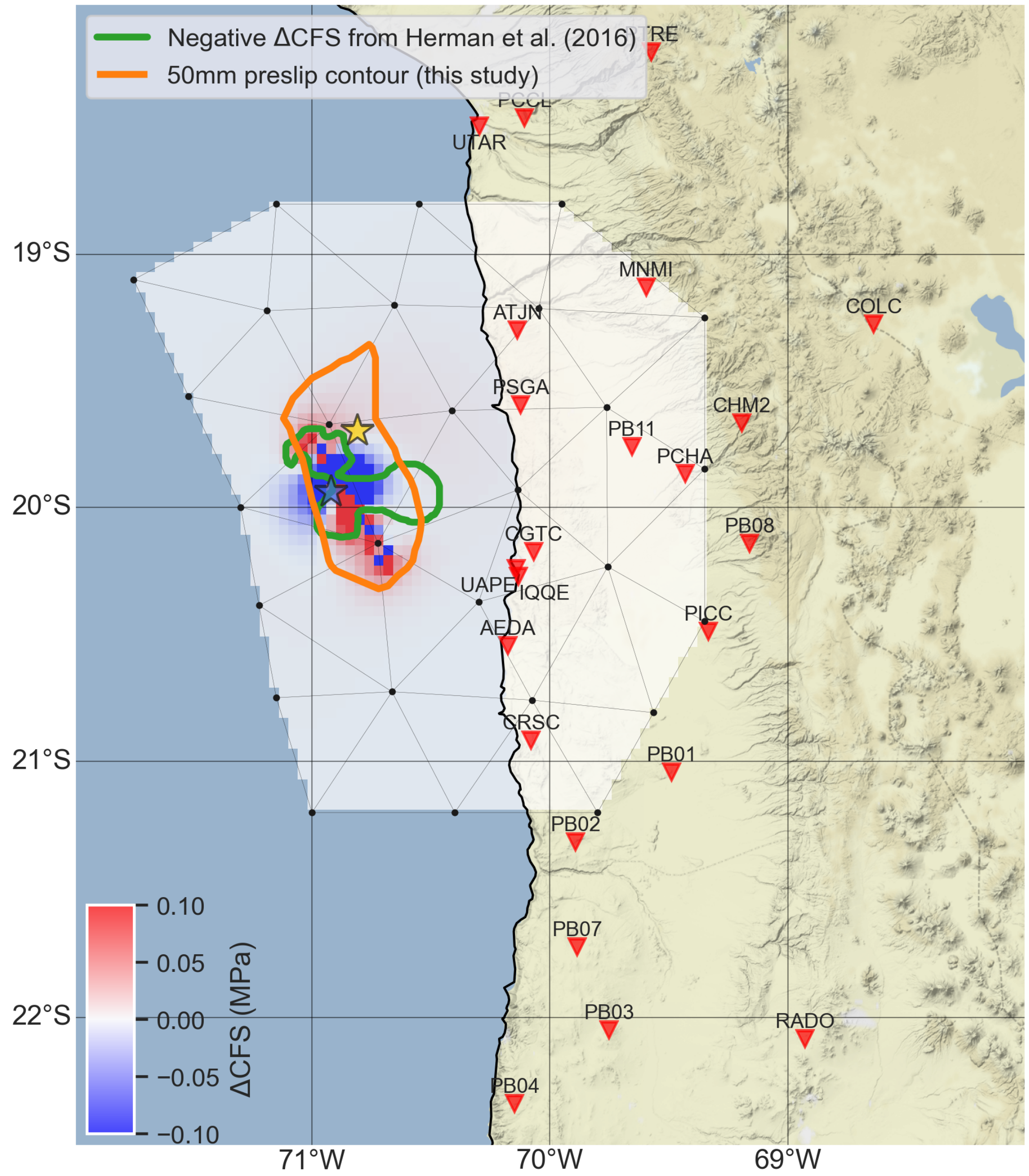

Figure 7. Map showing the static Coulomb stress changes induced by the largest foreshock (M_w6.7), which occurred on the overriding plate. This is calculated using the slip distribution obtained by Ruiz et al. (2019). The blue star shows the epicenter of that foreshock while the yellow star shows the epicenter of the Iquique earthquake. We show with the orange line the region of significant aseismic preslip (>50 mm) obtained using the corrected data. The green line outlines the area of negative Coulomb stress change inferred by Herman et al. (2016) using all the foreshocks from the sequence.

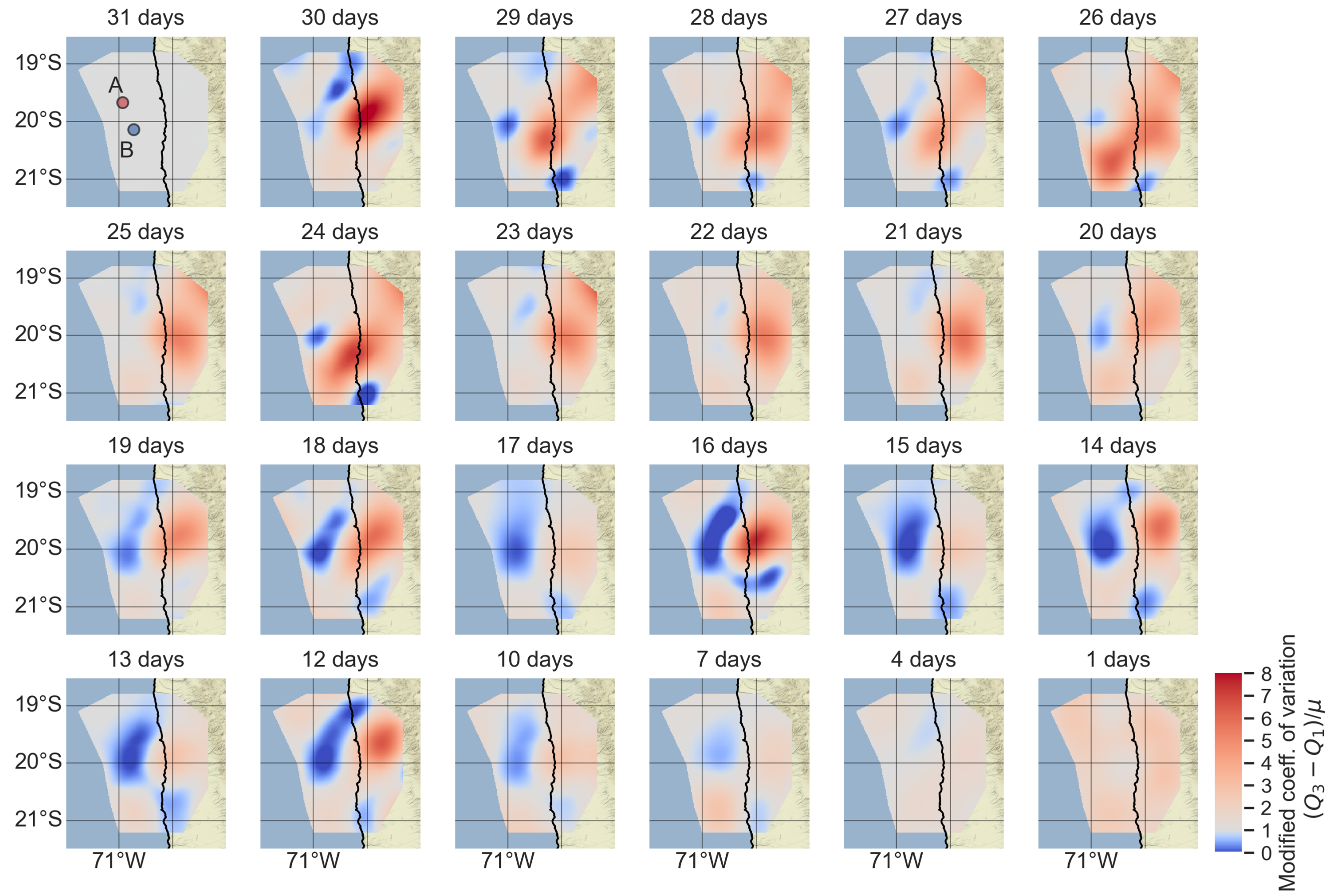

Figure 8. Spatial and temporal evolution of the modified coefficient of variation (i.e., difference between the third and first quartiles over the mode of the posterior probability density distributions). Cold colors are associated with values < 1, while warm colors are associated with a values > 1. The red and blue dots show the location of the nodes A and B, respectively, and displayed on Figure 9.

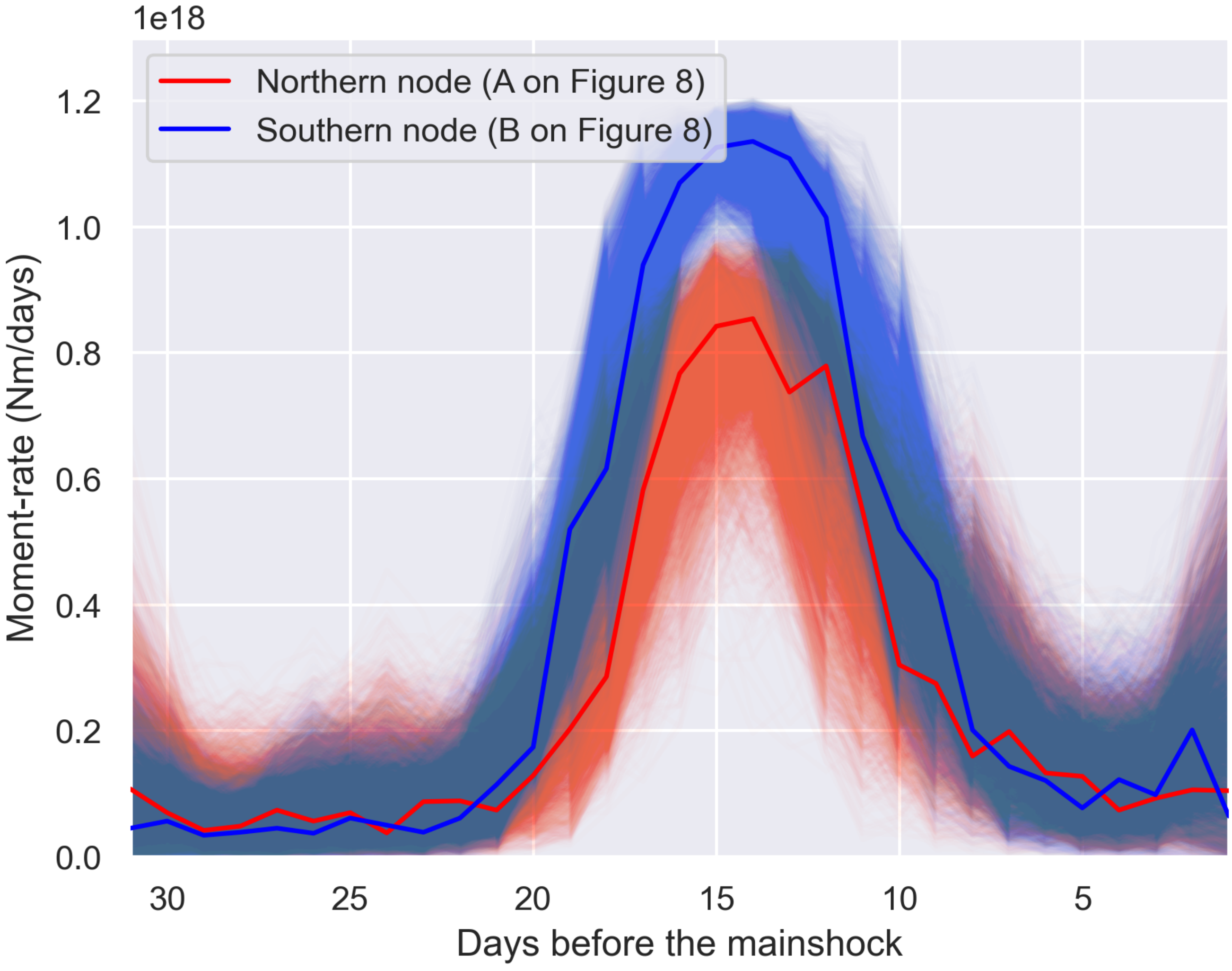

Figure 9. Temporal evolution of the moment-rate for the two nodes that experience the largest slip amplitude one the day before the earthquake. The thin lines are samples from the posterior probability density functions while the thick lines show the mode of the distributions.

Supplementary Materials

S1. Analysis of the spatiotemporal correlations of noise

As mentioned in the main text, we assume that the off-diagonal elements of the data covariance matrix are zero, meaning that there are no significant spatiotemporal correlations of the noise of the position time series. Here, we analyse this assumption in more details.

First, we can assume that there are no significant temporal correlations of noise. Indeed, as mentionned in the main text, since we use 31-days long time series, they are essentially dominated by white noise, which does not correlate. Therefore, we can only focus on the spatial correlations of the noise. To do so, we look at the correlations between the time series over the inter-seismic time period (i.e., from February 2011 to July 2013). For that, we split each time series into 31-days long time windows. Then, for a given time window, we compute the correlation coefficient for each possible pair of stations and treat the east and north component separately. We show how the correlation coefficients evolve as a function of inter-station distance (see Figure 10). We find that the correlation coefficients are significantly larger than 0, the point cloud being centerered around 0.5 with a standard deviation of about 0.2. However, we find no clear trend of the correlation coefficients as a function of the inter-station distances. Even though the best fitting curve (red line on Figure 10) shows a slight decrease, the spread of the data points implies a large uncertainty about this trend. Thus, the fact that the correlation coefficients do not depend on the inter-station distance suggests that this spatially correlated noise is caused by the presence of common-modes.

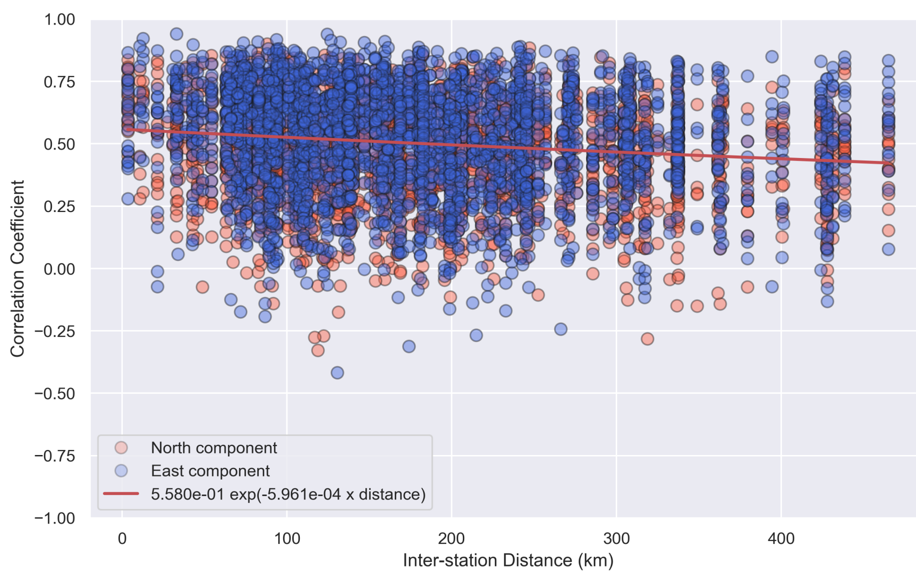

Figure 10. Correlation coefficients between two distinct time series for a given 31-days time window as a function of the inter-station distance. The blue dots are for the east component and the red dots are for the north component. The red line shows the best fitting curve with the form $A.\exp{(B.x)}$.

To investigate the presence of common-modes, we perform a principal component analysis (hereafter called PCA) over the interseismic time period. Because the time series contain gaps, we use the Probabilistic PCA from Porta et al. (2005). We find that only the first two components exhibit a coherent signal across the entire network (see Figure 11). The spatial pattern of each component is represented by vectors whose amplitudes range between 1.2 and 2.2 mm for the first component and between 0.5 and 3.0 mm for the second component (see bottom-row of Figure 11). These are the maximum amplitudes that the common-modes can potential reach. These are often larger than the values used to filled the diagonal elements of $\mathbf{C}_d$ ($\lesssim$ 1 mm). But, we can argue that they are small relatively to the signal from the initiation phase of the Iquique earthquake, which exceeds 5 mm for stations with a visible transient signal over the 1-month period that precedes the future mainshock. In addition, these vectors are modulated by their respective time functions (top row of Figure 11). Thus, to check what is the most likely contribution of the common-modes on our time series, we split the time function of each component into 31-days long time windows. Then, we compute the mean and standard deviation of each window, and obtain a mean close to 0.0 and a standard deviation of about 0.25 for each component. Therefore, we conclude that it is most likely that the amplitude of these two common-modes do not exceed 0.50 and 0.75 mm for component $\#1$ and component $\#2$, respectively. It could still be argued that common-modes could be accounted for by introducing off-diagonal elements on the data covariance matrix. But, this is already done since the used covariance matrix is a combination of $\mathbf{C}_d$ and $\mathbf{C}_p$, the latter containing off-diagonal elements that are of the order of the common-modes expected amplitudes.

From our investigation, we conclude that the time series contain common-modes, but (1) their likely amplitudes seems to be smaller than the noise of the time series, (2) some level of spatial correlations is already accounted for by the off-diagonal elements of Cp and (3) as the common-modes affect all stations at the same time, the effect would be to bias all patches the same way, which would not affect substancially the results. Therefore, we decide to not attempt removing the common-modes from the time series.

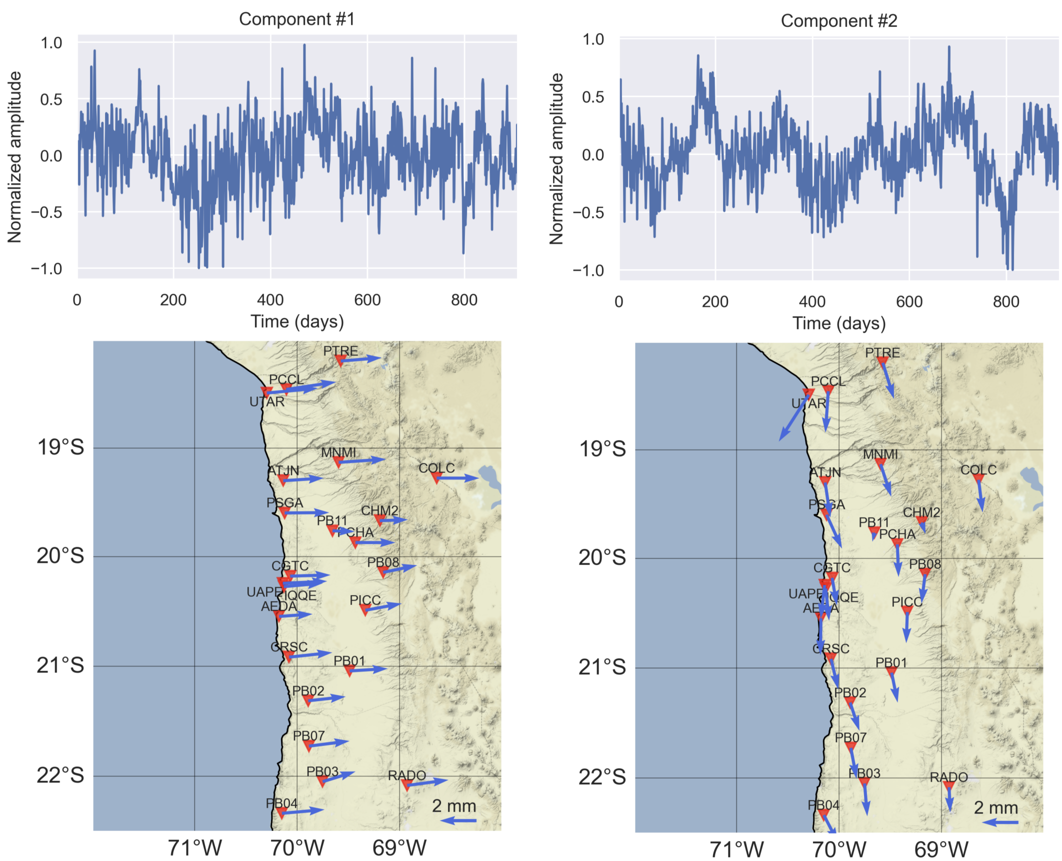

Figure 11. The 2 components of the PCA that are coherent accross the entire network. The top row shows the normalized time evolution of each component. The bottom row shows the amplitude and direction of each component. The scale of the vectors is shown on the bottom-right of the maps.

S2. Fit to the data

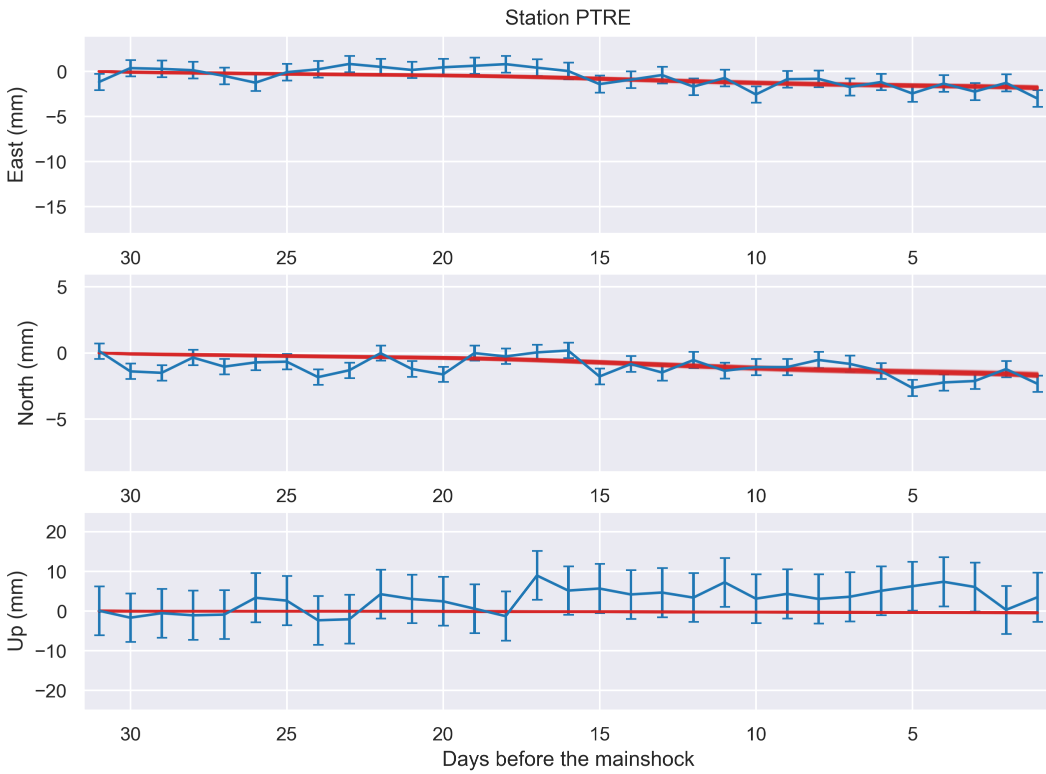

Figure 12. Comparison between the corrected time series (blue) and the predicted surface displacements for the aseismic preslip models (red). The top figure is for the east-component, the middle figure is for the north-component, and the bottom figure is for the vertical-component, although the latter is not used during the inversions. Stations are ranked from north to south. A map of the stations can be found on Figure 1a. The same scale is used by all figures and it is based on the extrema observed over the whole dataset.

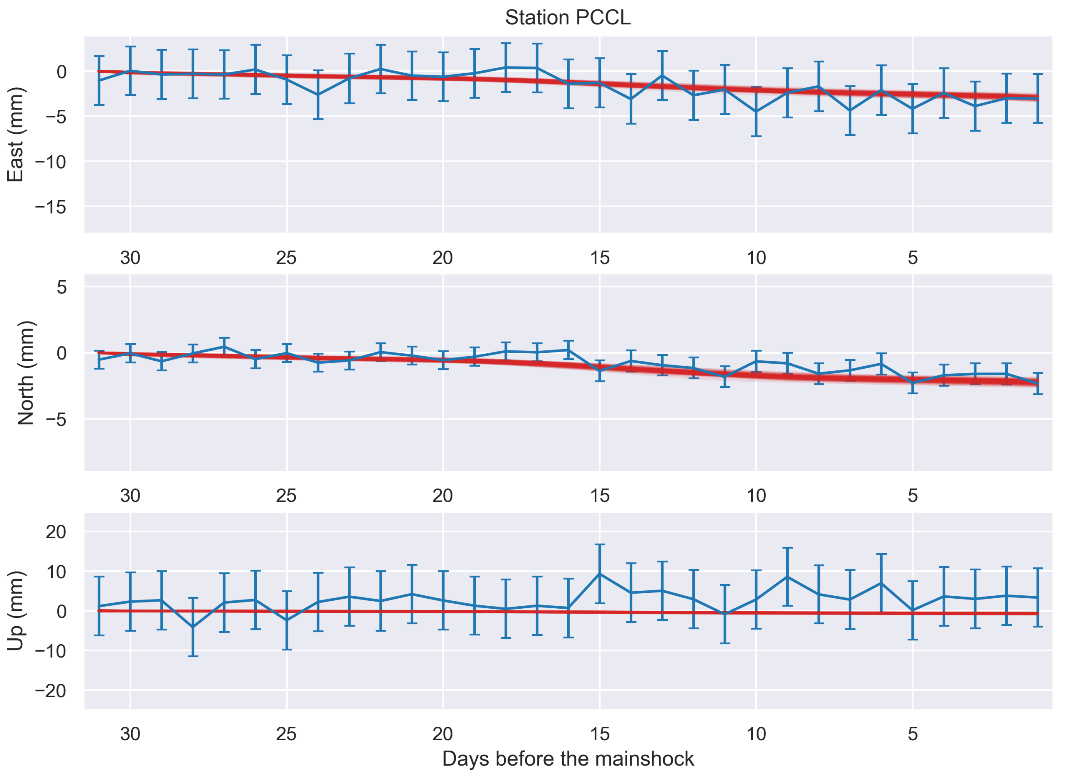

Figure 13. Same as Figure 12.

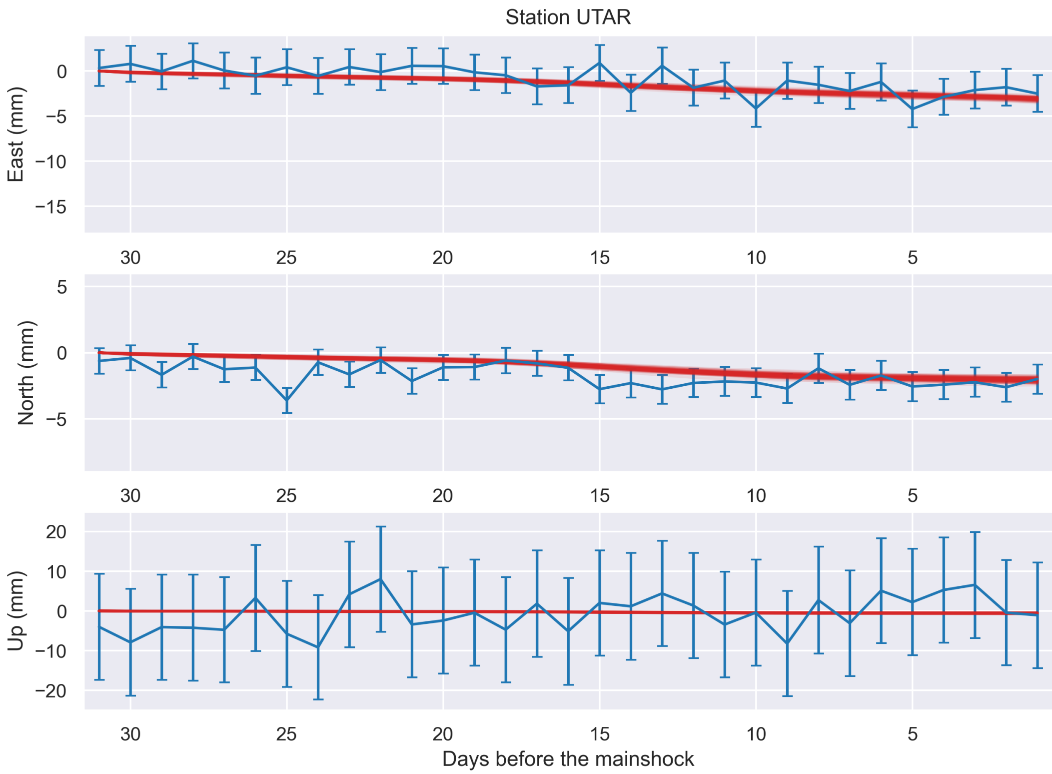

Figure 14. Same as Figure 12.

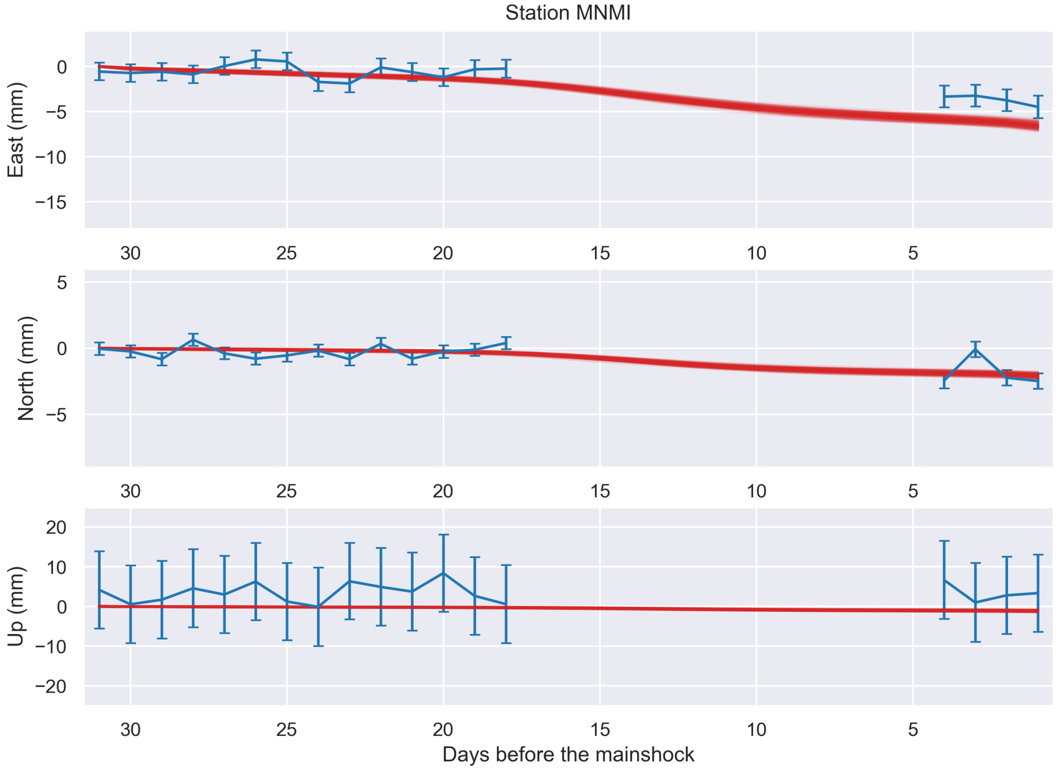

Figure 15. Same as Figure 12.

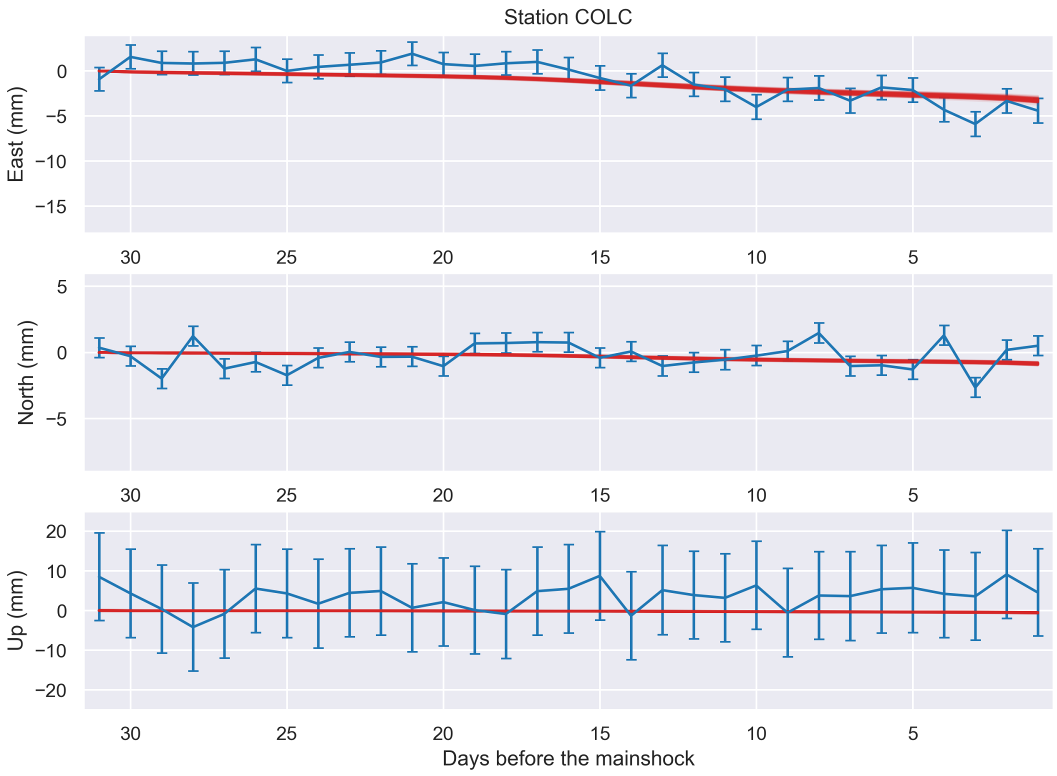

Figure 16. Same as Figure 12.

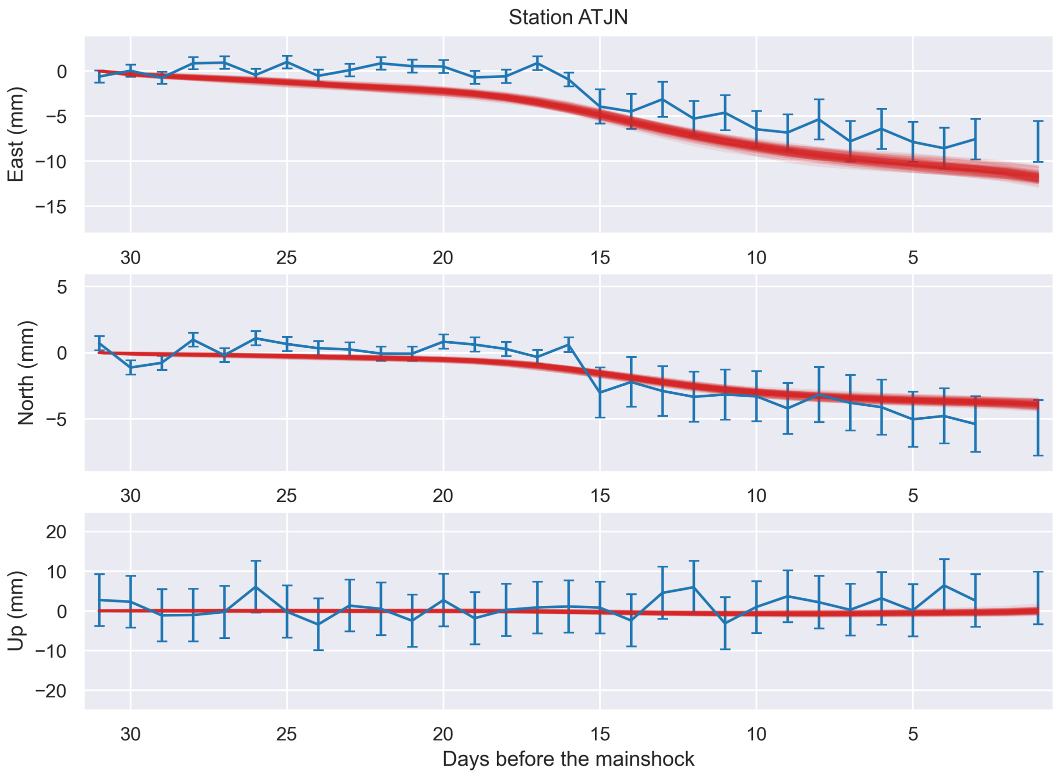

Figure 17. Same as Figure 12.

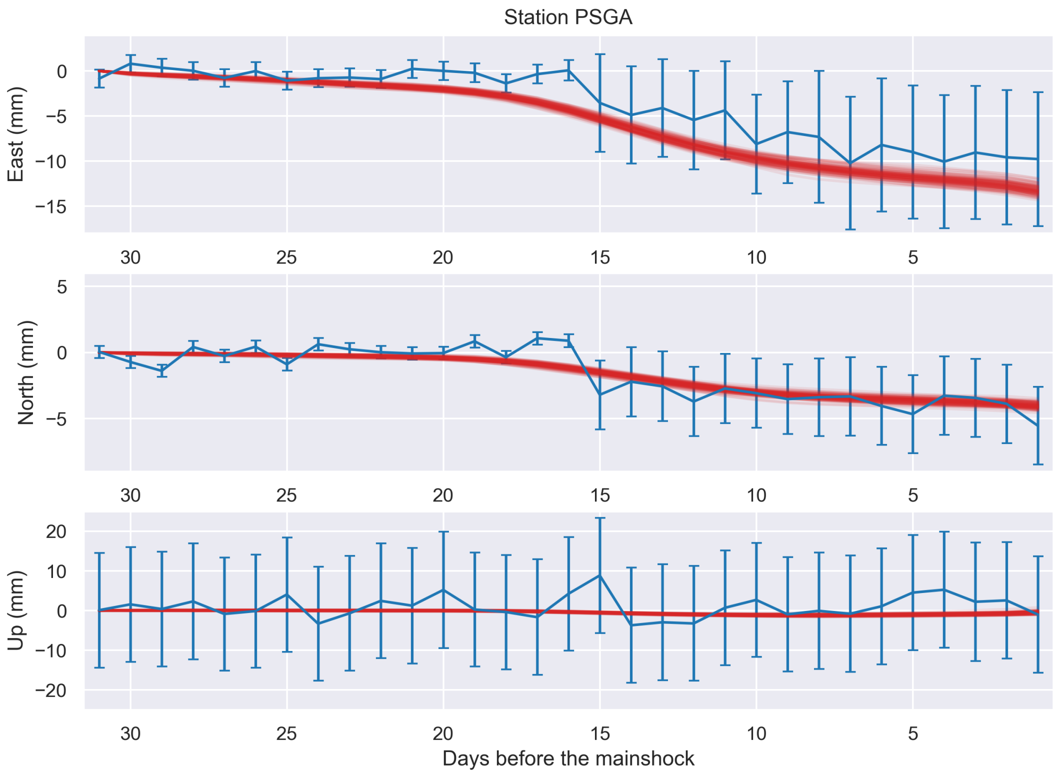

Figure 18. Same as Figure 12.

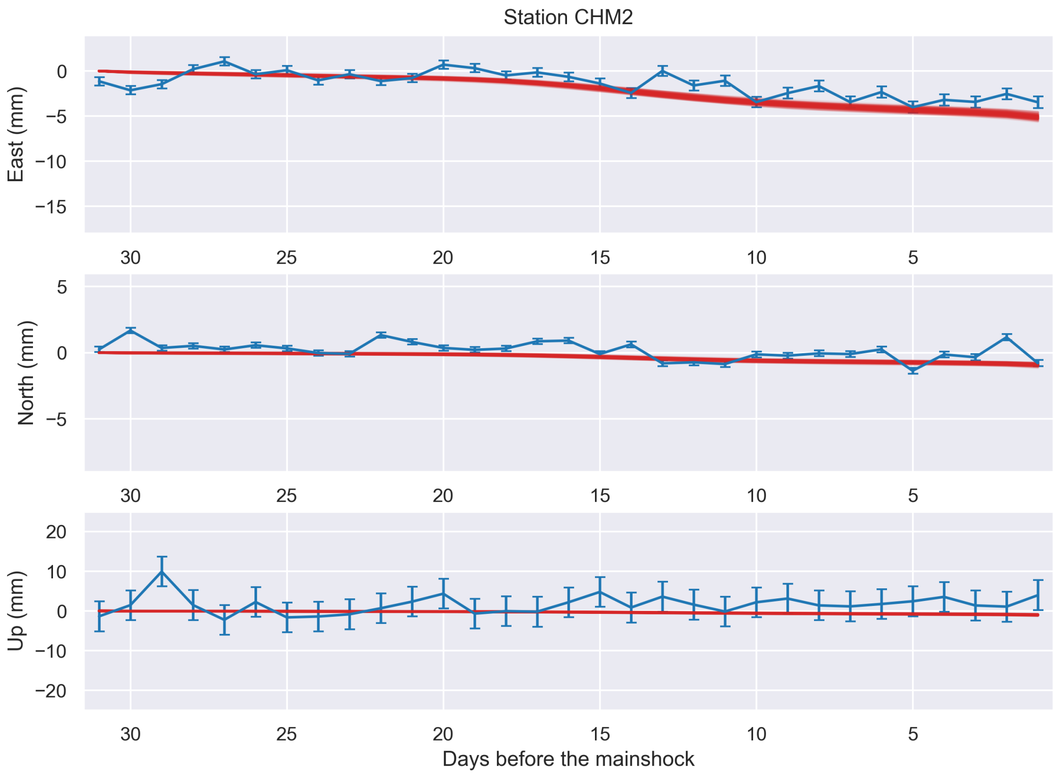

Figure 19. Same as Figure 12.

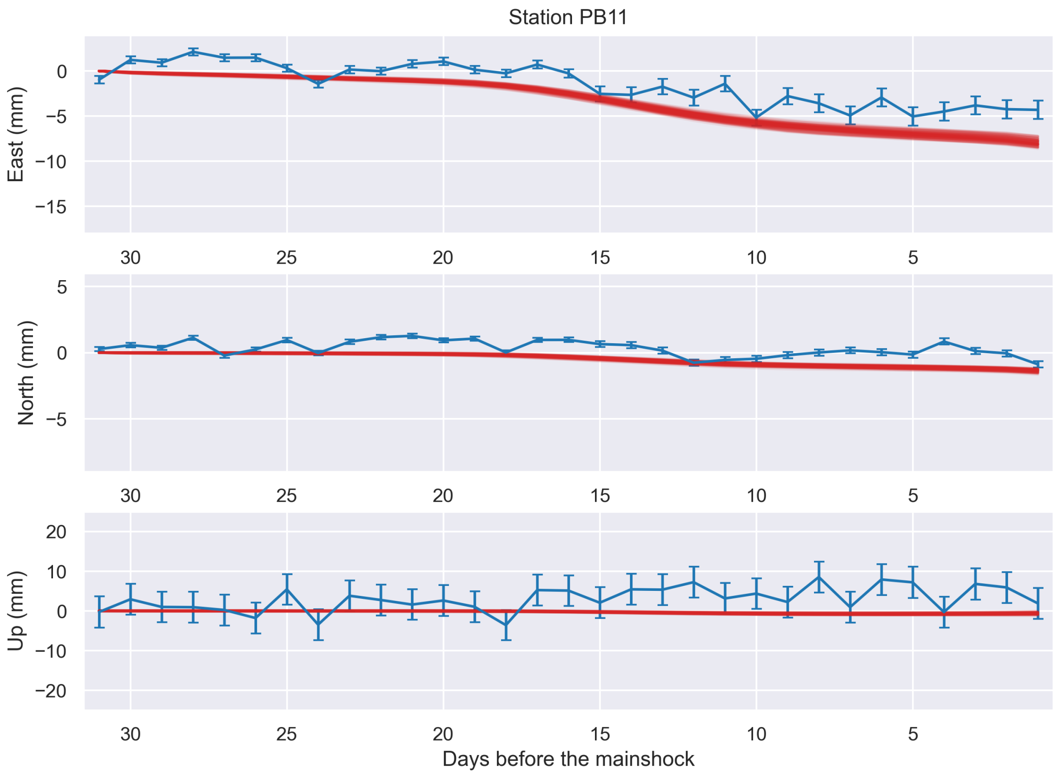

Figure 20. Same as Figure 12.

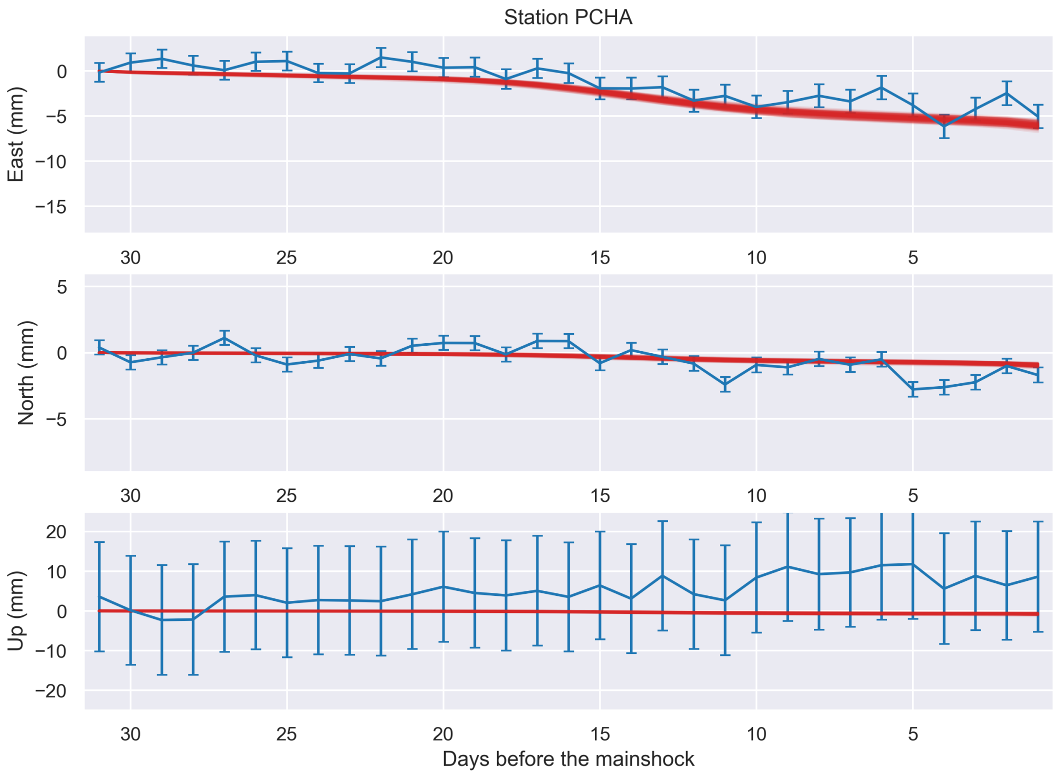

Figure 21. Same as Figure 12.

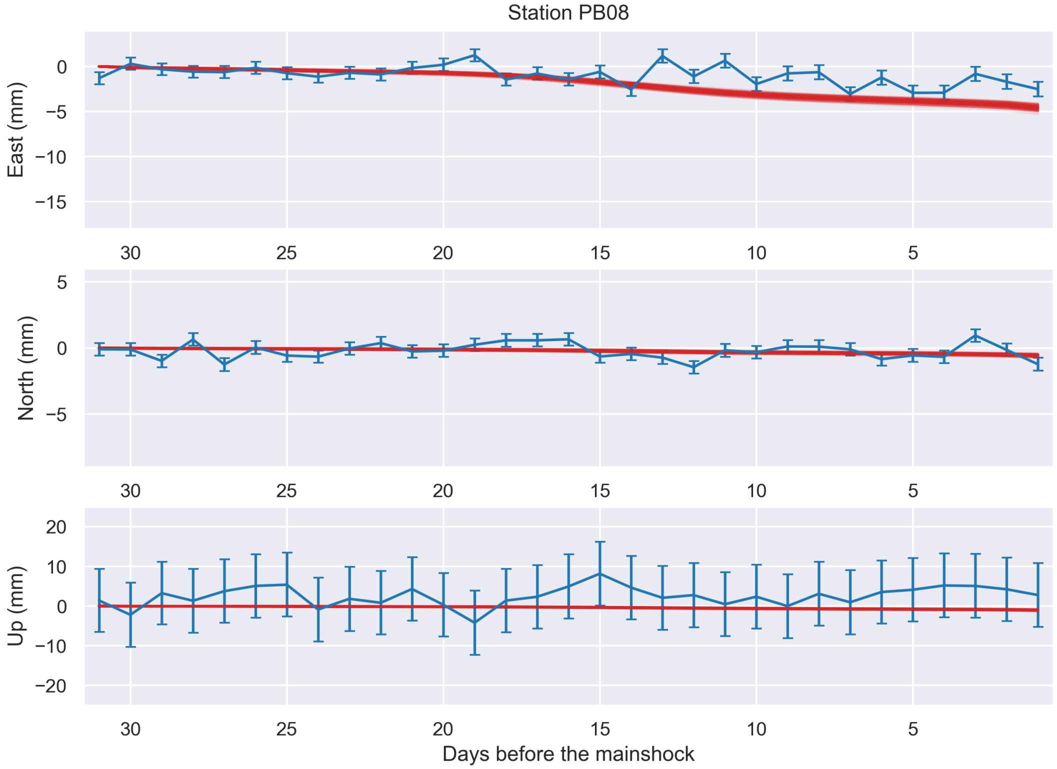

Figure 22. Same as Figure 12.

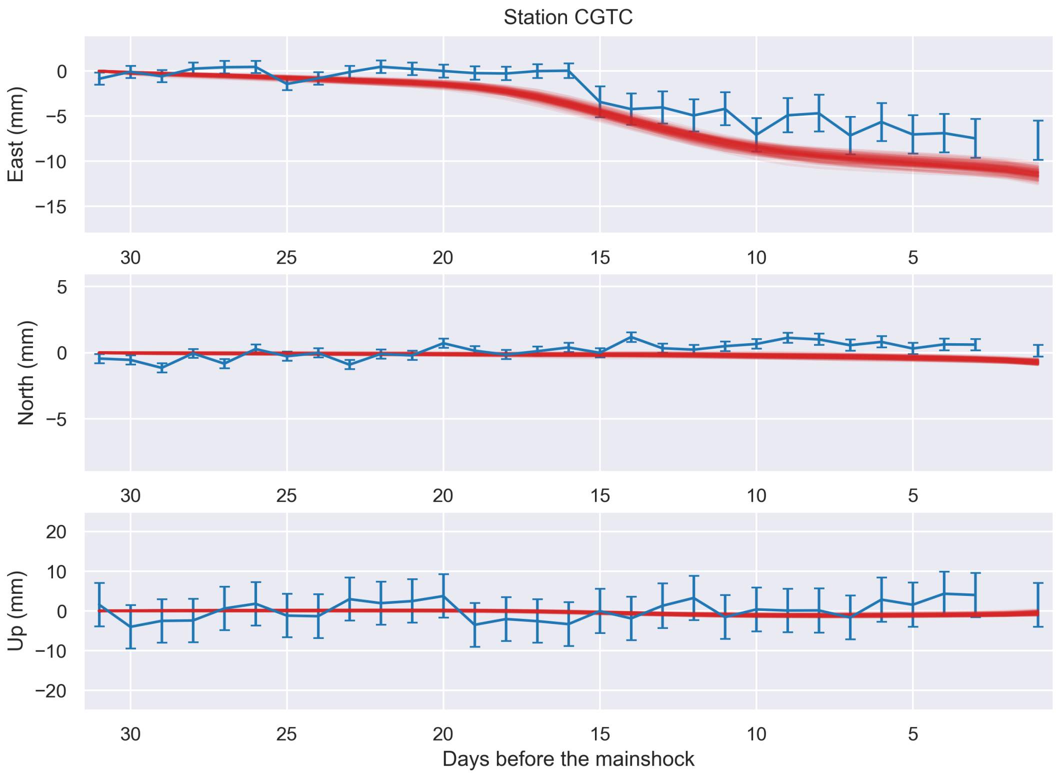

Figure 23. Same as Figure 12.

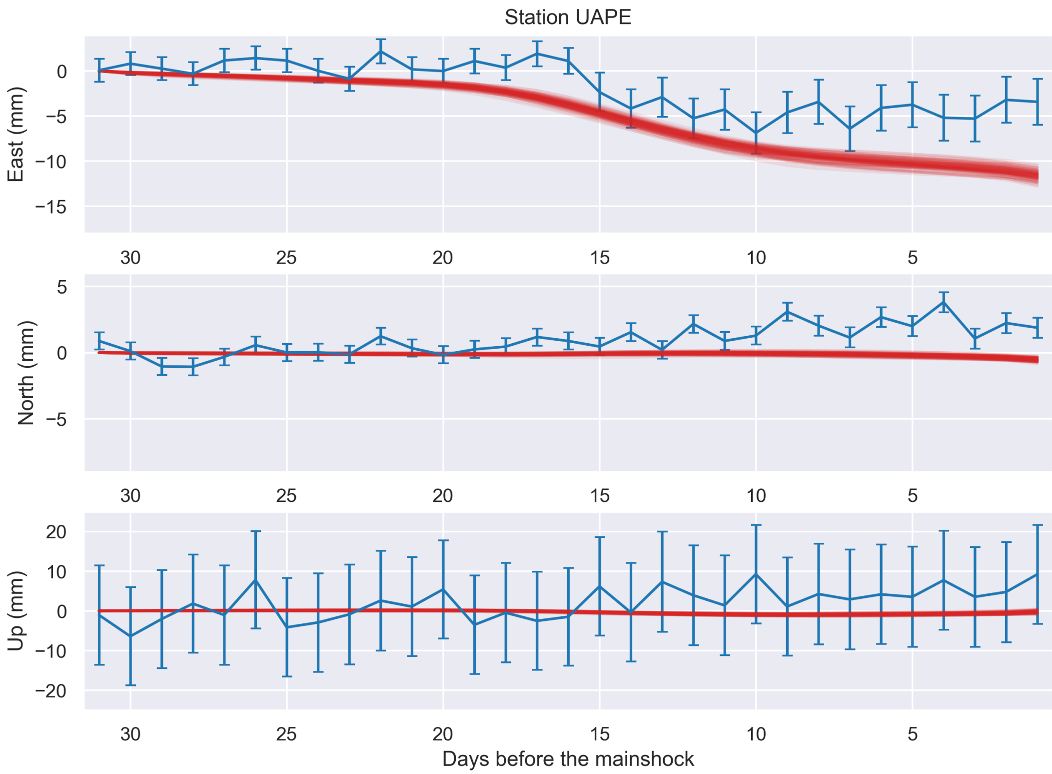

Figure 24. Same as Figure 12.

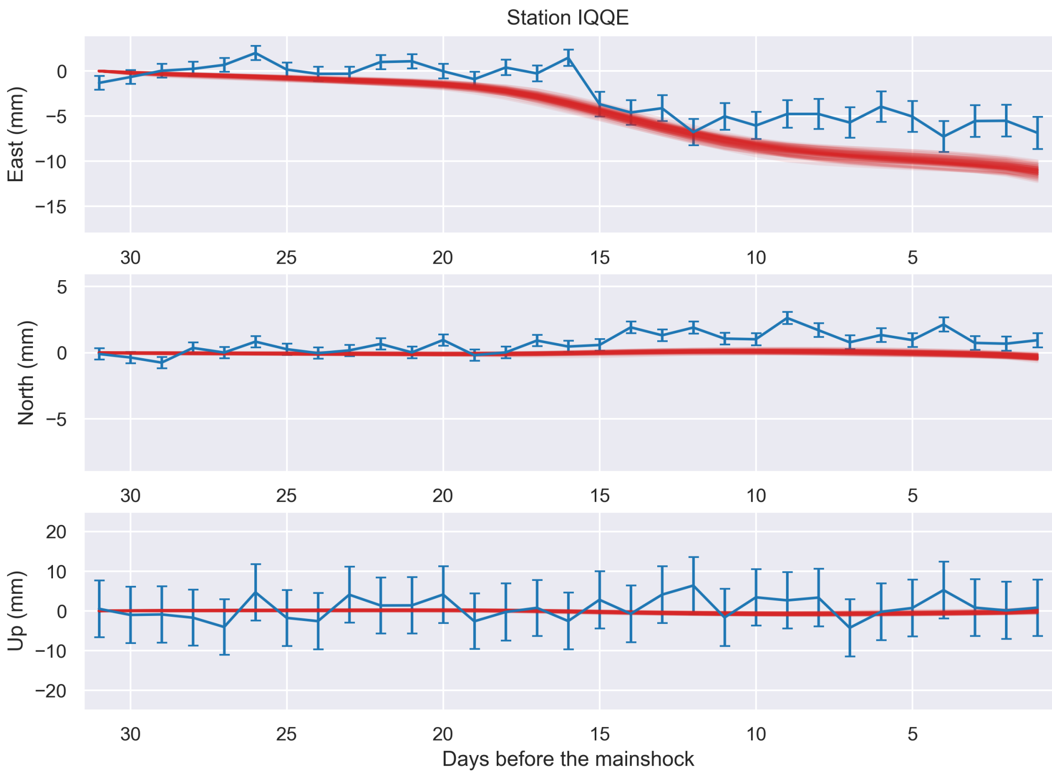

Figure 25. Same as Figure 12.

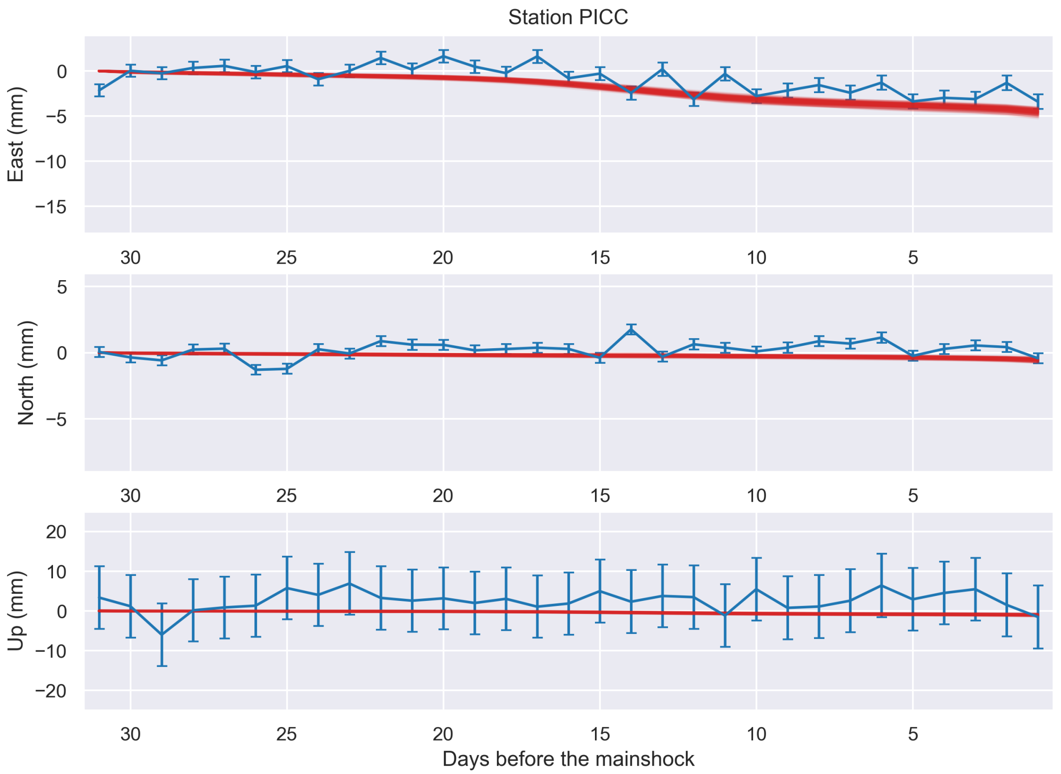

Figure 26. Same as Figure 12.

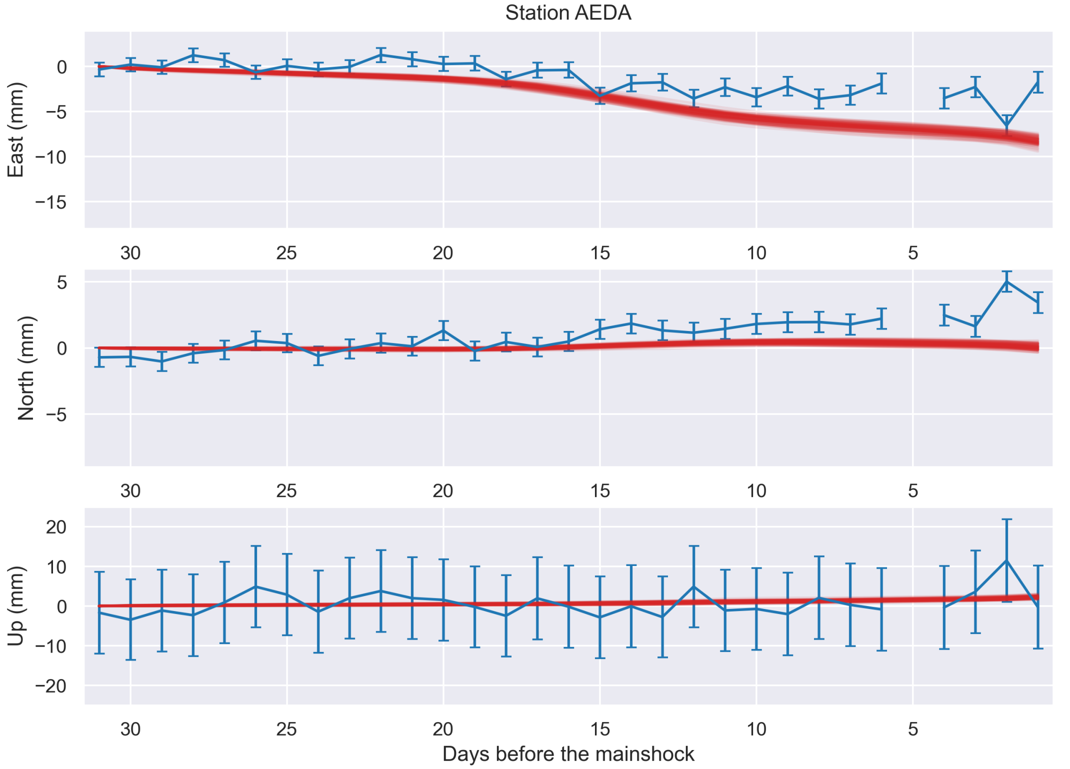

Figure 27. Same as Figure 12.

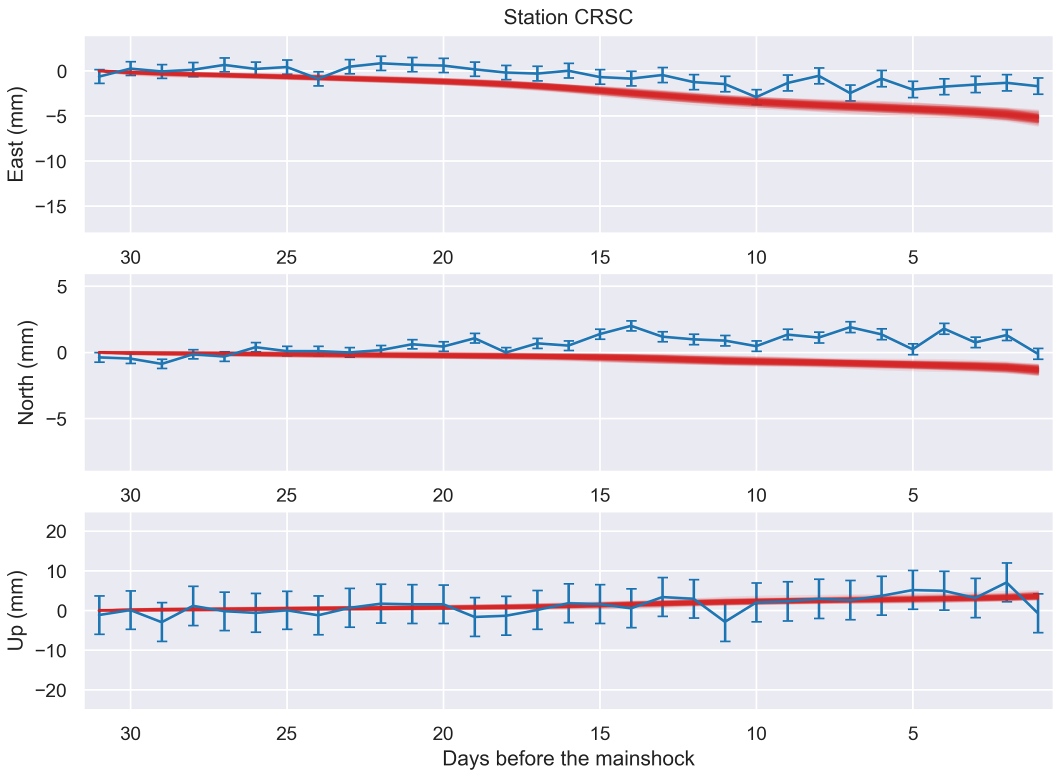

Figure 28. Same as Figure 12.

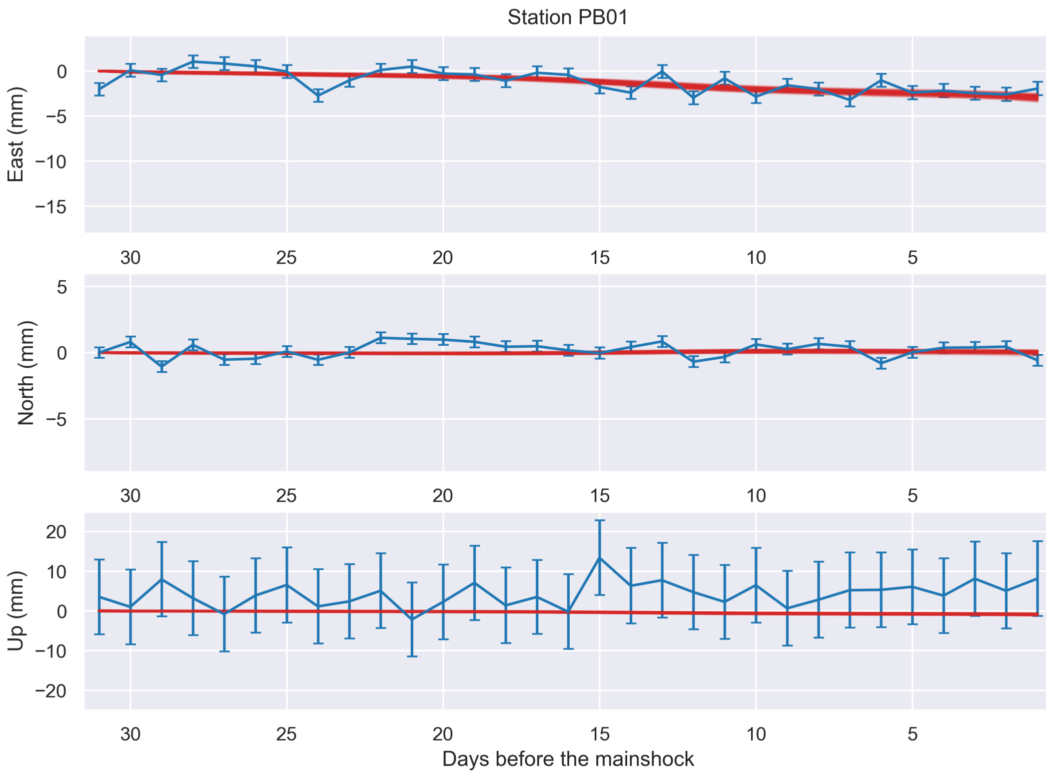

Figure 29. Same as Figure 12.

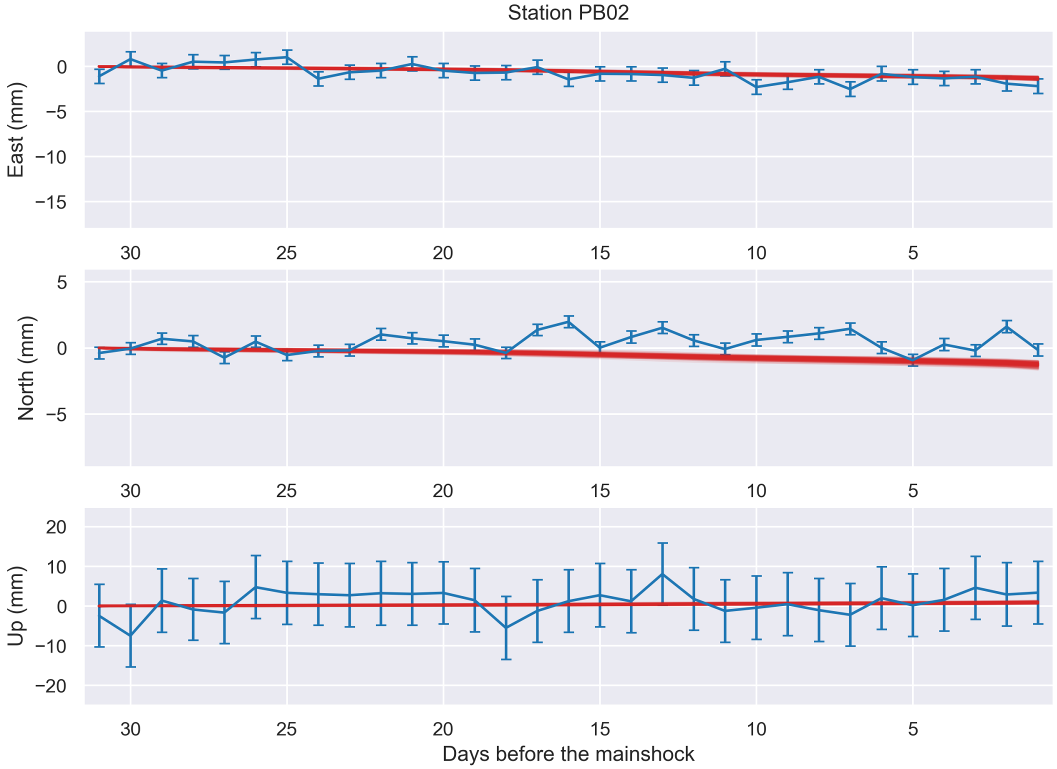

Figure 30. Same as Figure 12.

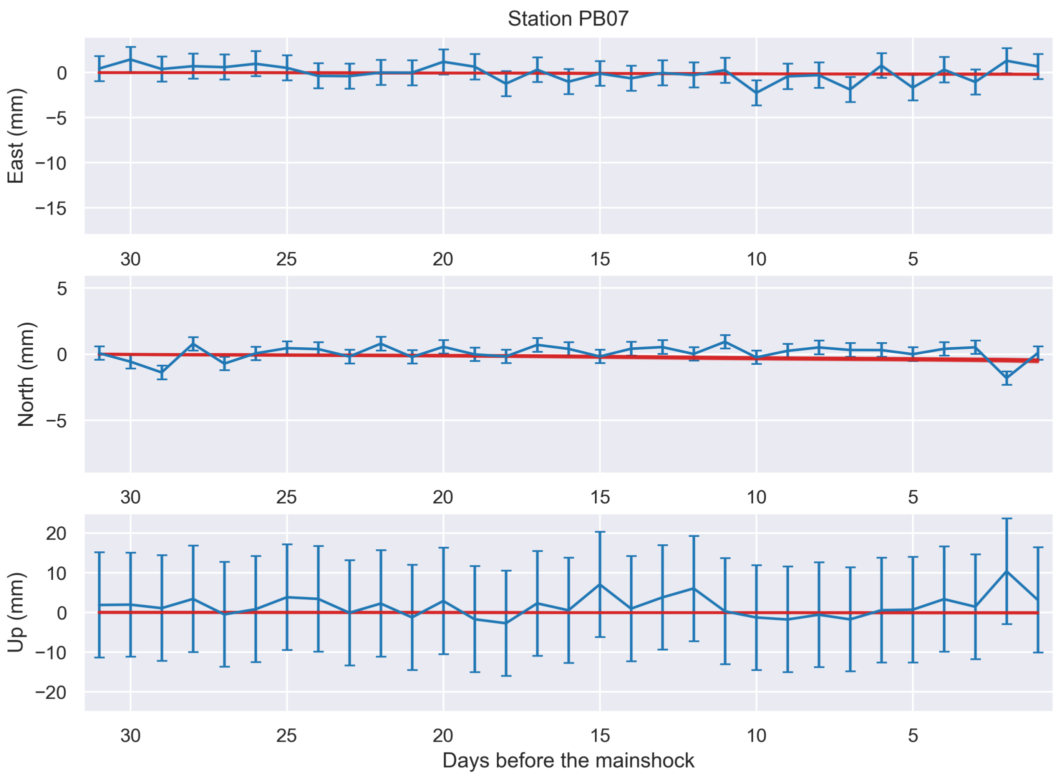

Figure 31. Same as Figure 12.

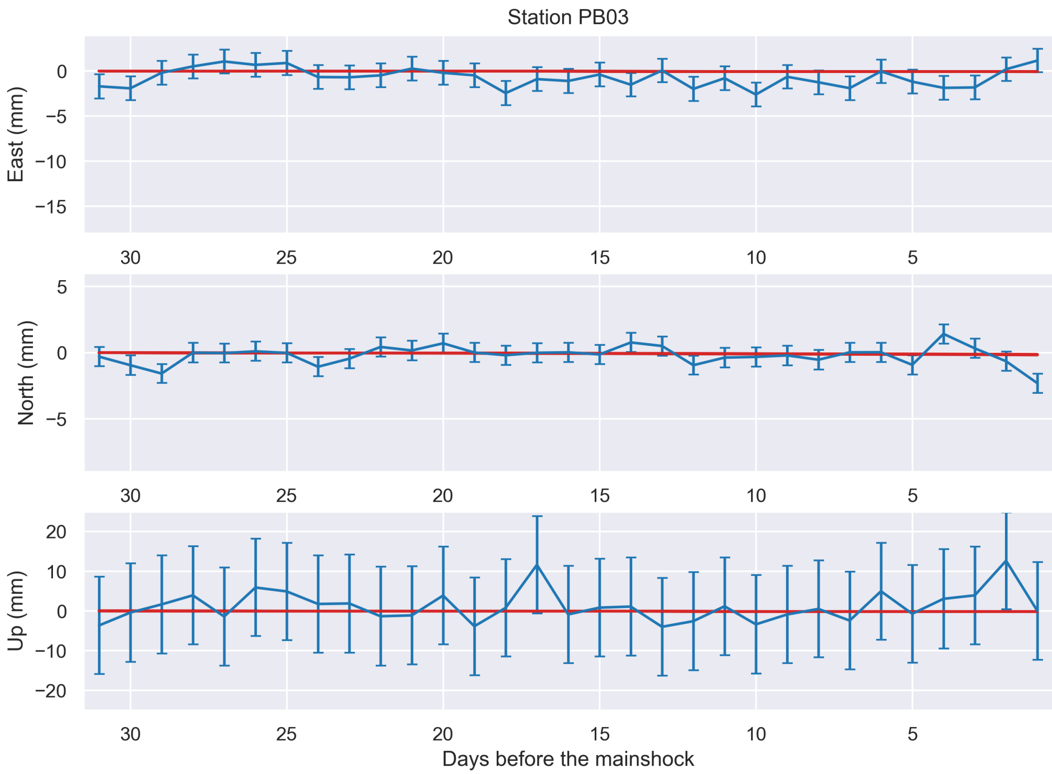

Figure 32. Same as Figure 12.

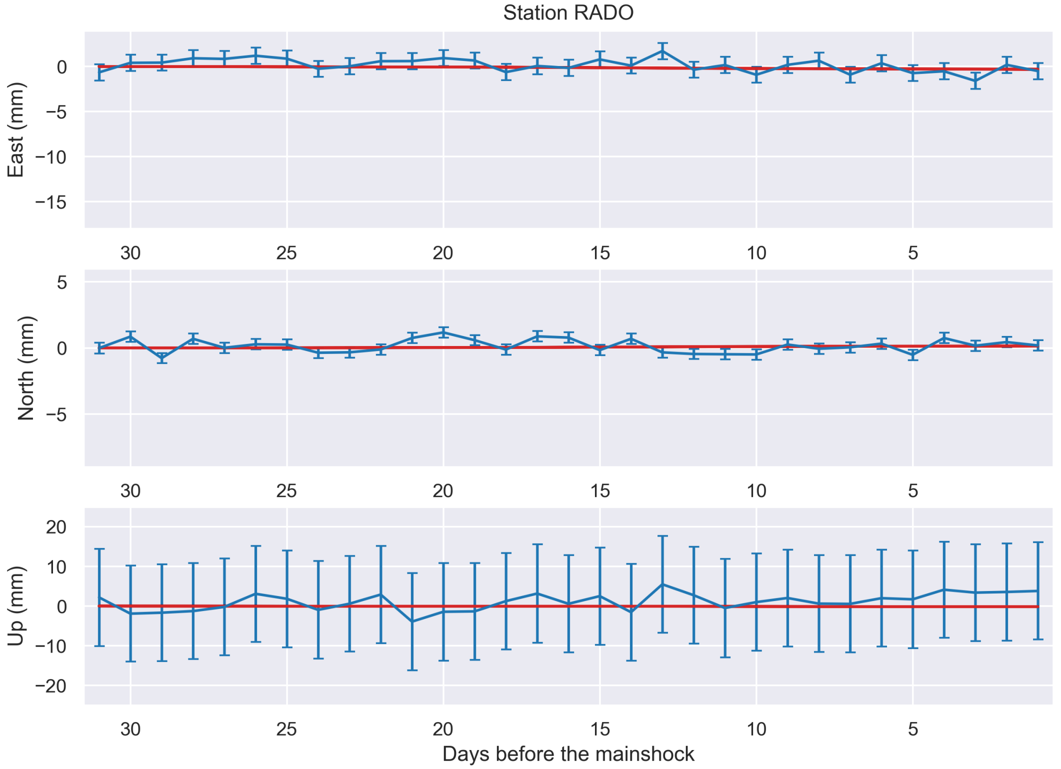

Figure 33. Same as Figure 12.

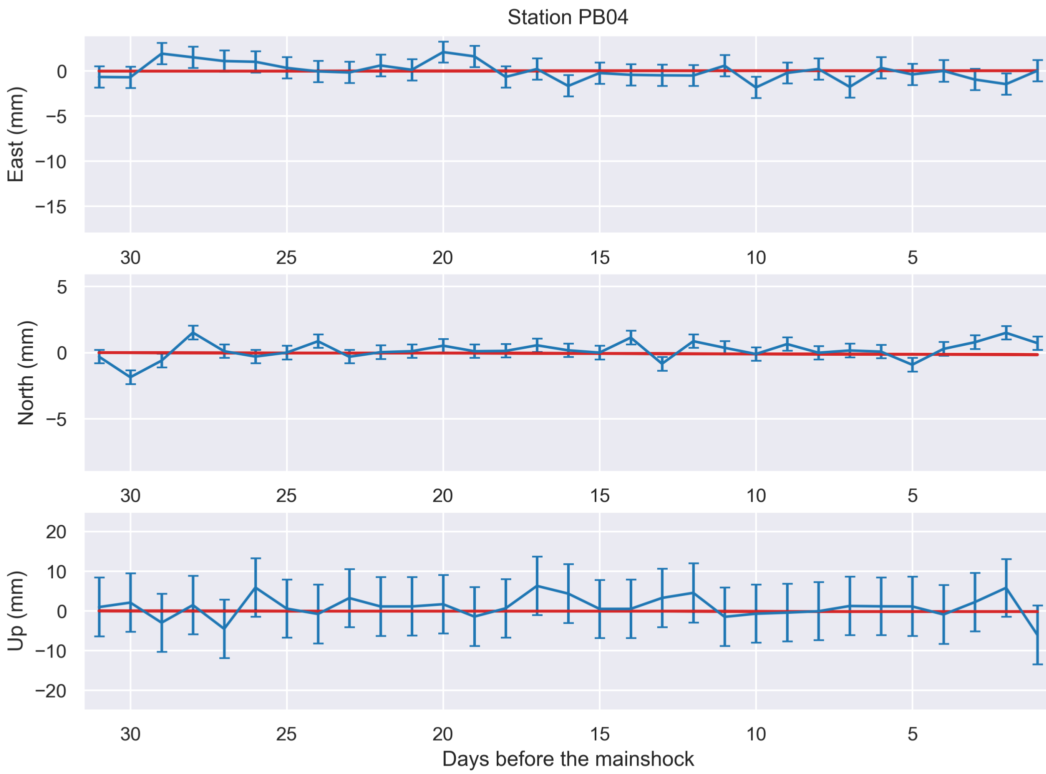

Figure 34. Same as Figure 12.

S3. Tilt records at Santa Rosa

We compute the tilt generated by the aseismic preslip distribution on the day prior to the mainshock (see Figure 3a) at the tiltmeter located in Santa Rosa, Chile (-20.171°N, -70.073°E). The tilt is computed using the following formulas:

$$\mathrm{tilt}_{EW} = -\frac{\partial u_z}{\partial x} \qquad \mathrm{tilt}_{NS} = -\frac{\partial u_z}{\partial y} \tag{6}$$

where u_z represents the vertical displacement (positive in the up-direction) while x and y represents the east-west and north-south direction, respectively. The partial derivatives are computed using a forward finite-difference approach using the vertical displacement predicted at the receiver itself as well as the vertical displacement predicted for two additional receivers, one located 0.01° north of Santa Rosa and one located 0.01° east of it. The vertical displacements are computed using the same velocity model as the one used to obtain the preslip models. This is different from Boudin et al. (2019) who use an elastic homogeneous half-space. We also compute predictions using many preslip models extracted from the posterior probability density functions so that we can get the uncertainties associated with our predictions. The results are shown on Figure 35. We find that tilt_{EW} is -11.5 $\mathrm{nrad} \pm$ 7.5 and that tilt_{NS} is 50.0 $\mathrm{nrad} \pm$ 4.0. These estimates barely exceed the uncertainty level given by Boudin et al. (2019) for the event that they label E4, which is the one we are interested in this study (48 and 42 nrad for the north and east components, respectively).

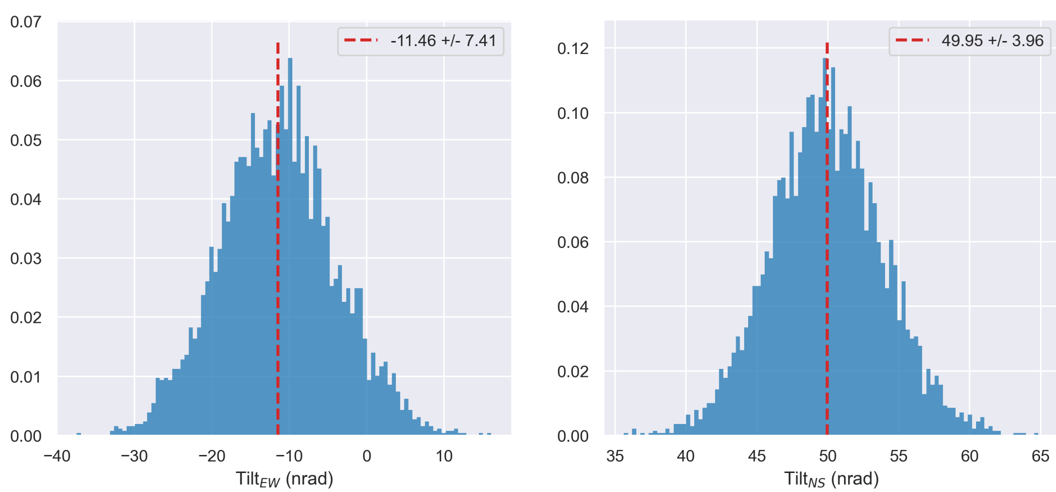

Figure 35. (left): probability density for the predictions of the tilt on the east-west component for various preslip models on the day prior to the future mainshock extracted from the posterior probability density functions. (right): probability density for the predictions of the tilt on the north-source component for various preslip models on the day prior to the future mainshock extracted from the posterior probability density functions. For both figures, the red dashed line shows the mean value from the distribution.